

Aeroelastic modelling of insect flight

B.Tech. Project Report

by

Nithin Adidela

160030026

Revanth Sharma

160030027

Faculty Adviser

Dr. Sudhakar Yogaraj



School of Mechanical Sciences

Indian Institute of Technology Goa

Declaration

We declare that this written submission represents our ideas in our own words and where others' ideas or words have been included, we have adequately cited and referenced the original sources.

We understand that any violation of the above will be cause for disciplinary action by the Institute and can also evoke penal action from the sources which have thus not been properly cited or from whom proper permission has not been taken when needed.

Nithin Adidela

160030026

Revanth Sharma

160030027

Date: July 1, 2021

Abstract

The aspect of insect flight is still a mystery to physicists and biologists. According to conventional aerodynamic theories, the small size of insects hinders their flight. Most theories assume a quasi-steady flow which fails due to high wingbeat frequency in insects. This implies that the insect flight is highly unsteady. Three important unsteady aerodynamic mechanisms associated with flapping wings are delayed stall, rotational circulation, and wing-wake capture. Quasi-static studies involving these three unsteady mechanisms are being conducted, although most of them assume a rigid wing. Apart from being elastic, the wing is made up of anisotropic material, further complicated by veins in its structure. Therefore, to develop a complete model, we need to understand how elasticity affects insect flight.

The focus of this project is to understand how wing flexibility affects aerodynamic forces and flow fields in insect flight. We employ a strongly coupled partitioned scheme to simulate the interaction between incompressible viscous fluid flow and a compressible solid, using open-source tools. Navier-Stokes equations describing fluid flows are solved using OpenFOAM, structural dynamics equations are solved using CalculiX and the coupling between these tools is achieved using preCICE.

In the first half of the project, quantitative validation of the solvers and the coupling library is conducted. The ability of the fluid solver to compute incompressible viscous flow under steady, unsteady conditions is tested by simulating the flow over a circular cylinder. Force coefficients, Strouhal number for unsteady cases are compared with literature. The fluid solver's ability to predict the aerodynamic forces and flow structures for a pitching airfoil performing fast acceleration is performed and validated against standard data. The accuracy of the structural FEM solver to predict the deflection of a cantilever beam loaded at its tip under small-deflection, large deflection with geometric non-linearity is verified. To validate the coupling, the behaviour of a flexible bottom attached to a lid-driven cavity with an opening and an unsteady inlet is simulated and verified. Grid independence is achieved for all the aforementioned simulations. The robustness of the coupling library is tested by simulating Turek-Hron FSI benchmark under steady as well as unsteady conditions with the density of solid close to that of the fluid.

In addition, in the second half of the project studies were conducted using overset meshes to validate the cases of Fruitfly kinematics (with grid independency) and simulated dragonfly kinematics. Currently, models are being built to conduct flexibility studies on these cases as well as the accelerated translation case, in order to understand the correlation between wing flexibility and aerodynamic force production.

Contents

1	Introduction	1
1.1	Why Study Insect flight?	1
1.2	Theory	1
1.3	Conventions and terminology	2
1.4	Quasi-steady modelling of Insect flight	3
1.5	Experimental challenges	4
1.5.1	Numerical Approaches and CFD for insect flight	4
1.6	Unsteady mechanisms in insect flight	5
1.6.1	Clap-and-fling	5
1.6.2	Delayed stall and the leading-edge vortex	5
1.6.3	Added mass	6
1.6.4	Rotational circulation	6
1.6.5	Wing-wake interactions – translational motion	6
1.6.6	Importance of flexibility	7
1.7	Objective	10
1.8	An overview of the open source tools used	10
2	FSI strategy, Overset meshes and validations	11
2.1	Governing Equations	11
2.2	Algorithm	12
2.3	Overset meshes	13
2.3.1	Overview	13
2.3.2	Comparison with conventional moving meshes	13
2.4	Fluid solver validation studies using standard test cases	15
2.4.1	Flow over a circular cylinder	15
2.4.2	Laminar flow around an airfoil	19
2.4.3	Accelerating airfoil	21
2.5	Structural dynamics solver validation studies using standard test cases	23
2.5.1	Small deflection of a cantilever beam	23
2.5.2	Large deflection of a cantilever beam involving geometric non-linearity	24
2.6	Coupling library validation studies using standard test cases	26
2.6.1	Lid-driven cavity with elastic bottom	26
2.6.2	Elastic cantilever attached to a circular bluff body	31
3	Simulations of flapping Wing	41

3.1	Translating rigid wing	41
3.2	Translating flexible wing	42
3.3	Fruitfly Kinematics using overset mesh	43
3.4	Fruit fly kinematics using Arbitrary Mesh Interface	48
3.5	Dragonfly kinematics using a flatplate	54
3.6	Dragonfly kinematics using an ellipse	57
4	Conclusions	58
4.1	Conclusions	58

List of Figures

1.1	Visual depiction of Kutta condition	2
1.2	Description of translation, supination and pronation	3
1.3	Clap-and-fling visualization	5
1.4	Leading-edge vortex	6
1.5	Wing venation	7
2.1	Active, Interpolating and Passive cells	13
2.2	Domain for flow over cylinder	15
2.3	Mesh for cylinder cases	16
2.4	Vortex shedding for $Re = 100$	16
2.5	Force coefficients for $Re = 20$	17
2.6	Force coefficients for $Re = 40$	18
2.7	Force coefficients for $Re = 100$	18
2.8	Domain used for laminar flow over an airfoil	19
2.9	Visualization of the mesh	20
2.10	Comparison of force coefficients for laminar flow over the airfoil at $Re = 1000$	20
2.11	Domain used for accelerated airfoil	21
2.12	Comparison of force coefficients for accelerating airfoil at $Re=100$	22
2.13	Vorticity and comparison with Hamdani(2000)	22
2.14	Small deflection of a cantilever beam	23
2.15	Large deflection of a cantilever beam	25
2.16	Comparison of displacement history of the tip	25
2.17	Domain for Lid-driven cavity with elastic bottom	26
2.19	Comparison of deflection of the center of the elastic flap	27
2.18	Vorticity plots for Lid-driven Cavity with elastic bottom at various instances	28
2.18	Vorticity plots for Lid-driven Cavity with elastic bottom at various instances (cont)	29
2.18	Vorticity plots for Lid-driven Cavity with elastic bottom at various instances (cont)	30
2.20	Depiction of effect of Surface Normal Gradient Scheme on Numerical Stability	31
2.21	Domain for Elastic cantilever attached to a circular bluff body	32
2.22	Vorticity plots for FSI2 at various instances	34
2.22	Vorticity plots for FSI2 at various instances (cont)	35
2.23	Vorticity plots for FSI3 at various instances	36
2.23	Vorticity plots for FSI3 at various instances (cont)	37

2.24	Effect of surface normal gradient scheme on numerical stability	39
2.24	Effect of surface sormal gradient scheme on numerical stability (cont)	40
3.1	Domain used for accelerated flat-plate	41
3.2	Comparison of force coefficients, rigid wing vs flexible wing	43
3.3	Depiction of background mesh	44
3.4	Closeup of subsidiary mesh	44
3.5	Cells from the 2 overlapping meshes	45
3.6	Vorticity plots for one full stroke involving fruitfly kinematics	47
3.7	Comparision of force coefficients over one full-stroke	48
3.8	Mesh for fruitfly case with AMI	49
3.9	Vorticity plots at different times	50
3.9	Vorticity plots at different times(cont)	51
3.10	Results for the first flap cycle	52
3.11	Results for the second flap cycle	52
3.12	Results for the third flap cycle	53
3.13	Results for the fourth flap cycle	53
3.14	Results for the fifth flap cycle	54
3.15	Depiction of background mesh	54
3.16	Closeup of subsidiary mesh	55
3.17	Vorticity plots for one full stroke involving dragonfly kinematics	56
3.18	Depiction of background mesh	57
3.19	Closeup of subsidiary mesh	57

List of Tables

2.1	Quantitative validation of fluid solver with flow over a cylinder test	17
2.2	Quantitative validation of solid solver with small deflection of a cantilever beam	24
2.3	Quantitative validation of solid solver with large-deflection of a cantilever beam	25
2.4	Non-dimensional parameters	32
2.5	Symbols for Elastic cantilever attached to a circular bluff body	33
2.6	Quantitative validation of FSI1 with benchmark	33
2.7	Quantitative validation of FSI2 with benchmark	36
2.8	Quantitative validation of FSI3 with benchmark	38

Chapter 1: Introduction

Insects were some of the first organisms to develop flight abilities [1]. An insects' flight abilities not only help them to escape from predators, it also helps them to search for food sources, mates, and find other suitable places to colonize in a much quicker way compared to their flightless predecessors. Thus, over the years insects have adapted in such a way that their flight performance plays a significant role in its survivability. This dependence on flight performance has rendered the flight-related sensory, physiological, behavioral and biomechanical traits to be compelling illustrations of adaptations found in nature.

1.1 Why Study Insect flight?

With the development of MAVs (Micro Aerial Vehicles) and other aerial vehicles becoming common [2, 3, 4], the potential that the knowledge of insect flight can have is huge. For example, a MAV which is modelled on insect flight dynamics may generate higher forces and maybe more efficient due to wing-wake interactions and leading edge vortex effects. This may mean that future MAVs can have better range and can last longer on a single battery charge, some of the most important criteria when you are choosing MAVs in practical scenarios.

The characteristics of insect flight cannot be explained by standard aerodynamic theories like thin airfoil theory and blade element theory [5]. These conventional theories invoke quasi-steady assumption, which states that the instantaneous aerodynamic forces on a wing are equal to the forces on the wing undergoing steady motion under an identical angle of attack and with the same instantaneous velocity. This assumption becomes invalid due to large flapping frequency, high stroke reversal speed, and rotational motion of the wings.

Recently, there have been advances in technology and techniques like high-speed videography, digital particle image velocimetry, and powerful computers for capturing wing kinematics, quantifying flows, and simulation and analysis respectively have become more commonplace. This is evident considering Ellington's comprehensive survey methods in 1984 [5], and how Willmott and Ellington [6] worked on high-speed videography on the same in 1987. Overall technological development has made us refine the model(s) of insect flight dynamics, enabling us to eliminate certain assumptions [1]. This helps in building a more comprehensive model of insect flight.

1.2 Theory

The basics of aerodynamics depend on a few critical equations, employed for thin airfoils. The modified form of the equations after making some specific assumptions are explicitly mentioned in section 2.1. One important thing to consider on top of them is the 'Kutta condition', where the unique value of additional circulation due to viscosity ensures the fluid stream over the plate meets the fluid stream under the plate smoothly and tangentially at the trailing edge.

The ‘Kutta condition’ ensures the slopes of fluid streams above and below the wing surface are equal, and thus the vorticity at the trailing edge is zero. This means that the fluid doesn’t make any sharp turns at the trailing edge.

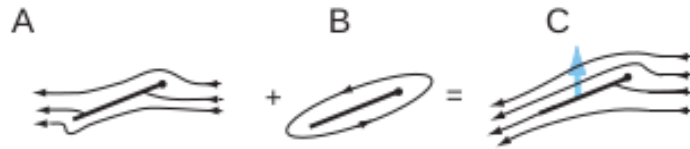


Figure 1.1: Visual depiction of Kutta condition [1]

In the presence of even the smallest amount of shear, the net aerodynamic force is usually perpendicular to the surface of the wing. The non-zero component of the force normal to the free-stream fluid motion is defined as ‘lift’ and the component parallel to the fluid motion is defined as ‘profile drag’. The component of drag due to viscous shear along the surface on an airfoil is called ‘viscous drag’.

1.3 Conventions and terminology

‘Wingspan’ refers to the length between the tips of the wings, when they are stretched out laterally. ‘Wing length’ refers to the base-to-tip length of one wing. ‘Wing chord’ refers to the section between the leading and trailing edge of the wing at any given position along the span. The ratio of span to mean chord is an important non-dimensional morphological parameter termed ‘aspect ratio’. ‘Angle of attack’ refers to the angle that the wing chord makes with the relative velocity vector of the fluid far away from the influence of the airfoil, i.e. relative to the ‘far-field flow’ or ‘free-stream flow’. This is also known as the ‘geometric angle of attack’. The ‘aerodynamic angle of attack’ refers to angle the wing chord makes relative to the locally deflected free stream. Because it is difficult to physically measure the down-wash related deflection of the free stream, most flight studies report geometric rather than aerodynamic angles of attack.

Because from one stroke to the next, insects rapidly alter many kinematic features that determine the time course of flight forces, including stroke amplitude, angle of attack, deviation from mean stroke plane, wing tip trajectory and wing beat frequency [7, 8], as well as timing and duration of wing rotation during stroke reversal [9]. Moreover, they may vary these parameters on each wing independently to carry out a desired maneuver. Hence, it is misleading to lump all patterns of insect wing motion into a single simple pattern. Mindful of this vast diversity in wing kinematics patterns, the wing motion of insects may be divided into two general patterns of flapping.

While hovering, most insects move their wings back and forth in a roughly horizontal plane, whereas others use a more inclined plunging stroke [5, 10]. Despite the predominance of the back-and-forth pattern, we use ‘upstroke’ and ‘downstroke’ to denote ventral-to-dorsal and

dorsal-to-ventral motion of the wing respectively.

It is important to note that as insects fly forward, their stroke plane becomes more inclined forward. The term ‘wing rotation’ will generally refer to any change in angle of attack around a chordwise axis. During the downstroke-to-upstroke transition, the wing ‘supinates’ rapidly, a rotation that brings the ventral surface of the wing to face upward. The wing ‘pronates’ rapidly at the end of the upstroke, bringing the ventral surface to face downward. ‘Flapping translation’ will refer to an airfoil revolving around a central axis, while ‘linear (or non-flapping) translation’ will refer to airfoils translating linearly.

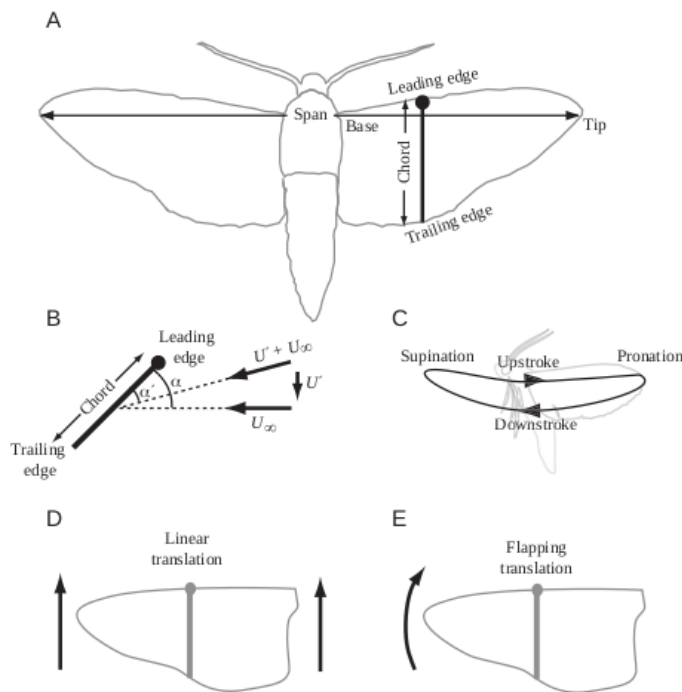


Figure 1.2: Description of translation, supination and pronation [1]

The term ‘finite wing’ refers to an actual 3D wing with two tips and thus a finite span length. While theoretical 2D wings can only create chord-wise flow, the wing tips in 3D wings creates a component of fluid velocity that runs along the span of the wing, perpendicular to the direction of far-field velocity during linear translation. Even though by definition 2D formulations cannot perform flapping motions, infinite wing assumption has often proved very useful in the study of animal flight, especially when wings have a high aspect ratio.

Within the context of force and flow dynamics, the term ‘steady’ signifies explicit time independence, whereas the word ‘unsteady’ signifies explicit temporal evolution due to inherently time-dependent phenomena within the fluid.

1.4 Quasi-steady modelling of Insect flight

In the hope of finding approximate analytical solutions to the insect flight problem, scientists have developed simplified models based on the quasi-steady approximations. According to the

quasi-steady assumption, the instantaneous aerodynamic forces on a flapping wing are equal to the forces during steady motion of the wing at an identical instantaneous velocity and angle of attack [5]. It is therefore possible to divide any dynamic kinematic pattern into a series of static positions, measure or calculate the force for each and thus reconstruct the time history of force generation. By this method, any time dependence of the aerodynamic forces arises from time dependence of the kinematics but not that of the fluid flow itself, which makes for simpler equations to calculate aerodynamic forces on insect wings.

Even though this model has been used with some success in the past [11, 12], this has not been able to account for the necessary mean lift when average flight force data are available. Ellington [5], in his comprehensive review of insect flight literature argued that if the maximum predicted lift predicted from the quasi-steady model was less than the mean lift required to hover, then the model had to be insufficient. This means that most of the forces generated cannot be accounted for by the quasi-steady effects alone, and we thus we have to look into unsteady mechanisms to explain the higher forces.

1.5 Experimental challenges

One of the greatest experimental challenges is how to visualize and quantify the wing motions of free-flying insects. *Drosophilamelanogaster* which is commonly referred to in both biological and physics experiments, is around 2-3 mm in length and flaps its wings at the rate of 200 Hz. The mere quantification of such an insect was a significant challenge, but with the advent of high-speed videography, we were able to provide more insight into the time course of the angle of attack and velocity of both wings [5, 6, 13].

Given the difficulties in directly studying insects or making theoretical calculations of their flight aerodynamics, many researchers have used mechanical models to study insect flight [14, 15, 16, 17]. While constructing the models, the Reynolds number and reduced frequency parameter (body velocity/wing velocity) of the mechanical model is matched to that of an insect, and is thus ‘dynamically scaled’. These studies are extremely useful in measuring flows and can thus provide benchmarks to be used in further studies. One of the most accurate ways to quantify the forces on the wings, however, was through computational fluid dynamics.

1.5.1 Numerical Approaches and CFD for insect flight

With advances in computational methods, and to overcome challenges for experiments, numerical simulations are becoming the norm to resolve the insect flight problem [18].

Using records that exist based on dynamically scaled models [15], there have been attempts to model the flight of *Drosophila*. Smith and others [15] modeled the flight of the hawkmoth using the unsteady aerodynamic panel method, which employs the potential flow method to compute the velocities and pressure on each panel of a discretized wing under appropriate boundary conditions. Liu and co-workers attempted to solve the full Navier-Stokes equation using ‘finite-volume-method’ [16, 19].

1.6 Unsteady mechanisms in insect flight

1.6.1 Clap-and-fling

The clap-and-fling is really a combination of two aerodynamic mechanisms. In some insects, the wings touch dorsally before they pronate to start the downstroke. This phase of wing motion is called ‘clap’. A detailed analysis of these motions in *Encarsia formosa* reveals that, during the clap, the leading edges of the wings touch each other before the trailing edges, thus progressively closing the gap between them. As the wings press together closely, the opposing circulations of each of the airfoils annul each other. This ensures that the trailing edge vorticity shed by each wing on the following stroke is considerably attenuated or absent. Because the shed trailing edge vorticity delays the growth of circulation via the Wagner effect[18]. The Wagner effect can be described in terms of circulation around any moving body as it suddenly starts its motion from rest, the circulation around the body reaches a steady-state only after the body has travelled several characteristic lengths. Weis-Fogh [20, 21] argued that the absence of trailing edge vortex would allow the wings to build up circulation more rapidly and thus extend the benefit of lift over time in subsequent stroke. In addition to the above effects, a jet of fluid excluded from the clapping wings can provide additional thrust to the insect [1, 5].

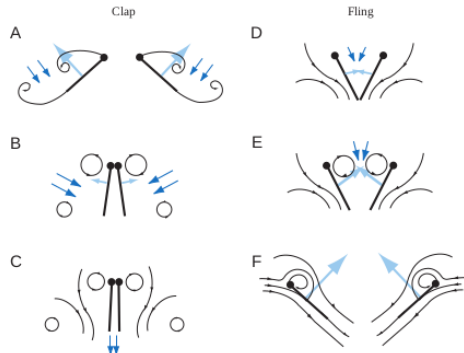


Figure 1.3: Clap-and-fling visualization [1]

At the end of clap, the wings continue to pronate by leaving the trailing edge stationary as the leading edges ‘fling’ apart. This process generates a low-pressure region between them, and the surrounding fluid rushes in to occupy this region, providing an initial impetus to the build-up of circulation of attached vorticity. The two wings then translate away from each other with bound circulations of opposite signs. Although the attached circulation around each wing allows it to generate lift, the net circulation around the two-wing system is still zero and thus conservation of circulation is satisfied. Collectively, the clap-and-fling could result in a modest, but significant, lift-enhancement.

1.6.2 Delayed stall and the leading-edge vortex

The major difference in the flight of an insect and an airplane is how the insect’s wings are angled in normal flight. During normal fixed-wing translation on an airplane, the wings lose

their ability to generate enough lift to fly at an angle of attack of 12 degrees, in a process described as ‘stalling’. However, an insect can achieve stable translational flight even at angles in excess of 45 degrees, and it does not stall. This is because, as the wing increases its angle of attack, the fluid stream going over the separates as it crosses the leading edge but reattaches before it reaches the trailing edge. In such cases, a leading edge vortex occupies the separation zone above the wing. Because the flow reattaches, the fluid continues to flow smoothly from the trailing edge and the Kutta condition is maintained. In this case, because the wing translates at a high angle of attack, a greater downward momentum is imparted to the fluid, resulting in substantial enhancement of lift. Experimental evidence and computational studies have identified this leading-edge vortex as the single most important feature of the flows created by insect wings and thus the forces they create [12, 22, 23].

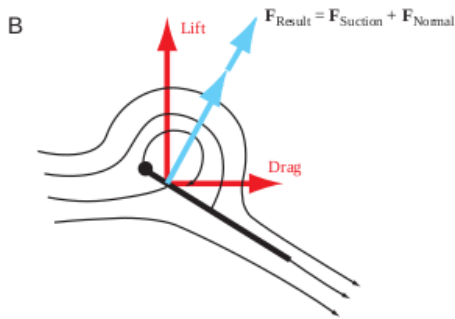


Figure 1.4: Leading-edge vortex [1]

1.6.3 Added mass

Unlike the forces mentioned in the previous section, an accelerating wing encounters a reactionary force due to the accelerated fluid. This reactive non-circulatory force [24] falls outside the realm of standard circulation-based steady-state analyses and is called ‘added mass’ [25]. This reactionary force causes adds to the lift during both the translational and the rotational motion of the wings

1.6.4 Rotational circulation

Unlike a normal fixed wing, an insect’s wing does not maintain a constant angle of attack. The wings on an insect rapidly change their inclination. In order to maintain the Kutta condition, addition circulation over the wings to counteract the rotation. This rotational circulation leads to a generation of lift [12, 26].

1.6.5 Wing-wake interactions – translational motion

The reciprocating pattern of wing motion used by insects suggests that their wings might potentially interact with the shed vorticity of prior strokes. As the wing reverses stroke, it sheds both the leading edge and the trailing edge vortices. These shed vortices induce a strong inter-vortex velocity field. As the wing reverses direction, it encounters the enhanced velocity and acceleration fields, thus resulting in higher aerodynamic forces immediately following stroke

reversal. This phenomenon has been called ‘wake capture’ or wing-wake interactions. The magnitude and relative strengths of the shed vortices, and therefore wake capture, are strongly dependent on the kinematics of the wing immediately before and after stroke reversal [11, 12, 26].

1.6.6 Importance of flexibility

All the studies mentioned above considered rigid wings. However, insect wings aren’t rigid. The insect wings are elastic in nature. The presence of wing veins is also an important characteristic that had not been considered in all rigid studies. Moreover, the wings are also anisotropic in nature, making it harder to model. All these criteria contribute to the kinematics and overall geometry of the wings, and can thus affect the aerodynamic forces generated by the flapping wings. Another important phenomenon to consider is the solid-fluid interactions between the wing surface and its surrounding air medium. All these ‘aeroelastic interactions’ are tough to model and is numerically intensive, as we have to ensure that the numerical models that we are using give us convergent solutions for both the solid and fluid case.

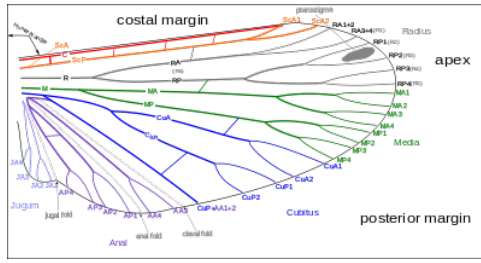


Figure 1.5: Wing venation

With proper empirical evidence [27], the aeroelastic effects are shown to strongly influence aerodynamic force generation. But there was no conclusion to be inferred regarding the aerodynamic mechanism involved in flexible wings, flexibility may not alter the basic aerodynamic mechanism during flapping (i.e. generation of leading edge vortex, which contributes to force enhancement), however because flexion of the trailing edge generates lower net forces than a rigid wing, the leading edge vortex for a flexible wing maybe probably smaller than its rigid counterpart, implying that the Kutta condition is established with relative ease when the flexible trailing edge realigns in the direction of the flow.

Further, from [28], we can see that wing deformation acts as a passive pitch (which is considered as an effective angle of attack), which can lead to positive lift, and thus add to forces accounted by quasi-steady and unsteady mechanisms. However, these studies considered the wing structure to be isotropic in nature. They are anisotropic in reality. Insect wings being flexible has received surprisingly less attention, even though it has been considered as an important factor for insect flight aerodynamics [29, 30]. However, studies have been done on the aeroelastic effects considering wings to be isotropic in nature. The flexural stiffness (EI) also varies over several orders of magnitude [31], from 4.39×10^{-6} in some insects to 8.23×10^{-4}

in others.

The rarity in research on the aspects of flexibility in dynamic fluid flow situations doesn't mean that there weren't any studies conducted. As far as in 2010, Zhao et al [32] conducted experimental studies on the aerodynamic effects of flexibility in flapping wings. This has set up a computational benchmark for further studies, with the experiment being carried out with various flexural rigidities of the wing and angle of attack. While it found that the flexion of the trailing edge caused the net forces to be lower than its rigid counterpart, there was no conclusion reached on whether flexibility does alter the basic aerodynamic mechanism during flapping. It also assumes that with the camber induced, there might be greater circulation and thus larger forces, however the isotropic wing structure which could not capture the deflections seen in anisotropic structures. Peng and Milano [33] also conducted experiments to see how an elastically mounted flapping plate's natural frequency would be related to its damping ratio. Here, a flatplate undergoes fixed sinusoidal translation along with rotation about its long axis. They showed that the stroke length plays a crucial role to determining forces, and phase differences in plate trajectory also play an important part in optimal lift generation. However, this study only considers passive pitching results. Liu et al [34] studied the aerodynamic effects of dynamic wing flexion in translating wings experimentally, with the help of digital particle velocimetry. Jin et al [35] studied the edge effects on low-aspect ratio flexible plates, using various tip geometries. In addition, Shinde, Arakeri [36] and Bluman et al [37] showed that flexibility plays a crucial role in thrust production in swimming and achieve hover equilibrium during flight respectively. These experimental studies all explore different cases where flexibility is shown to change previous models, but due to experimental constraints no in-depth experimental study is possible in these topics.

However, Yeh and Alexeev [38] performed FSI simulations and constructed a 3D fully coupled computational model to investigate free swimming and understand the basic physics of unsteady and undulatory locomotion. They used 3D lattice Boltzmann models to do force measurements. However, even they used an isotropic flat plate for the simulations. With this, again computational mechanics took a front step in the research front for insect flight this time including study of flexibility as well.

In the field of aerodynamics, Arora et al [39] analysed the role of chordwise passive wing flexibility in forward propulsion for low Reynolds number flows, using Lattice-Boltzmann method for fluid and Newton-Euler method for structural simulations, assuming that the flexibility was discrete. Over various Reynolds number flows and non-dimensional parameters used in FSI, they discovered that the effects of aerodynamics on bending is much lesser than the effects of inertia. However, they did not consider initial acceleration, and the study was conducted in 2D considering chordwise flexibility only.

Lastly, Lee et al [40] conducted studies on the changes in thrust and lift through changes

in the flexibility of the wing in hover forward flight. This study concluded that the thrust and lift coefficients obtained are much larger than those obtained with a rigid wing. They also found that the freestream interacts with the vortex system near the wing in forward flight, and also discovered that as the advance ratio increases (ratio of forward movement to the upward movement), the thrust and lift produced decreases. However, all these studies were conducted using an isotropic wing structure.

This study was started with a goal of finding the effect of flexibility on the aerodynamic forces and fields produced in insect flight by conducting FSI simulations using open-source tools. The tools were selected by keeping in mind that they can handle anisotropic materials in case the study were to extend into a 3 dimensional FSI study.

1.7 Objective

The broad objective of this project is to study how wing flexibility affects aerodynamic forces and flow fields generated by flapping wings. We will be using strongly coupled partitioned approach to solve the multiphysics problem, with the conforming mesh method. We aim to conduct these studies with the help of open-source solvers and couplers. We use a strongly coupled solver, in which fluid part is solved using OpenFOAM [41], the structural part is solved using CalculiX [42], and the coupling between the two is achieved using preCICE [43] tool. The ability of the solvers and coupler to conduct FSI simulations will be established by simulating and quantitatively validating several standard test cases. Upon validation, a 2 dimensional rigid wing will be developed which can perform flapping motion as in a fruitfly or a dragonfly. Flexibility studies will be conducted on a 2 dimensional isotropic wing performing a translating acceleration motion to study the effect of flexibility on delayed stall.

1.8 An overview of the open source tools used

An overview of the fluid solver, OpenFOAM v7 [41]

OpenFOAM [41] (Open-source Field Operation And Manipulation) is an opensource C++ toolbox which comes with a set of inherent customisable standard solvers aimed at solving continuum mechanics problems, mostly focused on computational fluid dynamics. It also involves pre and post-processing tools. The boundaries of what OpenFOAM can do can be stretched by adding several third party addons.

An overview of the solid solver, CalculiX [42]

CalculiX [42] is an opensource software aimed at solving field problems with the Finite Element Method. The package involves a pre- and post-processing tool called cgx which is used to build and analyse Finite Element Models. The package can solve both linear and non-linear problems in the static, dynamic and thermal domains.

An overview of the coupling library, preCICE [43]

preCICE [43] (Precise Code Interaction Coupling Environment) is a coupling library for partitioned multi-physics simulations. By partitioned, we mean that preCICE makes use of existing independent solvers working on solving problems in different domains and couples them to solve Multiphysics problems. There is no limitation on the type or the number of solvers that can be coupled using preCICE. It provides both implicit and explicit coupling schemes.

Chapter 2: FSI strategy, Overset meshes and validations

2.1 Governing Equations

Governing equations for the fluid

The flow of an incompressible viscous Newtonian fluid is governed by the following equations
Conservation of mass is governed by continuity equation

$$\frac{\partial v_i}{\partial x_i} = 0 \quad (2.1)$$

Conservation of momentum is governed by Navier-Stokes equation

$$-\frac{\partial p}{\partial x_i} + \mu^f \frac{\partial^2 v_i}{\partial x_j \partial x_j} = \rho^f \left(\frac{\partial v_i}{\partial t} + v_j \frac{\partial v_i}{\partial x_j} \right) \quad (2.2)$$

Governing equations for the solid

Equilibrium equation for a solid is given by

$$\frac{\partial T_{ij}^s}{\partial x_i} + \rho^s b_j = 0 \quad (2.3)$$

Constitutive equation for a linear elastic solid is given by

$$T_{ij}^s = C_{ijkl}^s E_{kl}^s \quad (2.4)$$

where, the infinitesimal strain tensor is given by

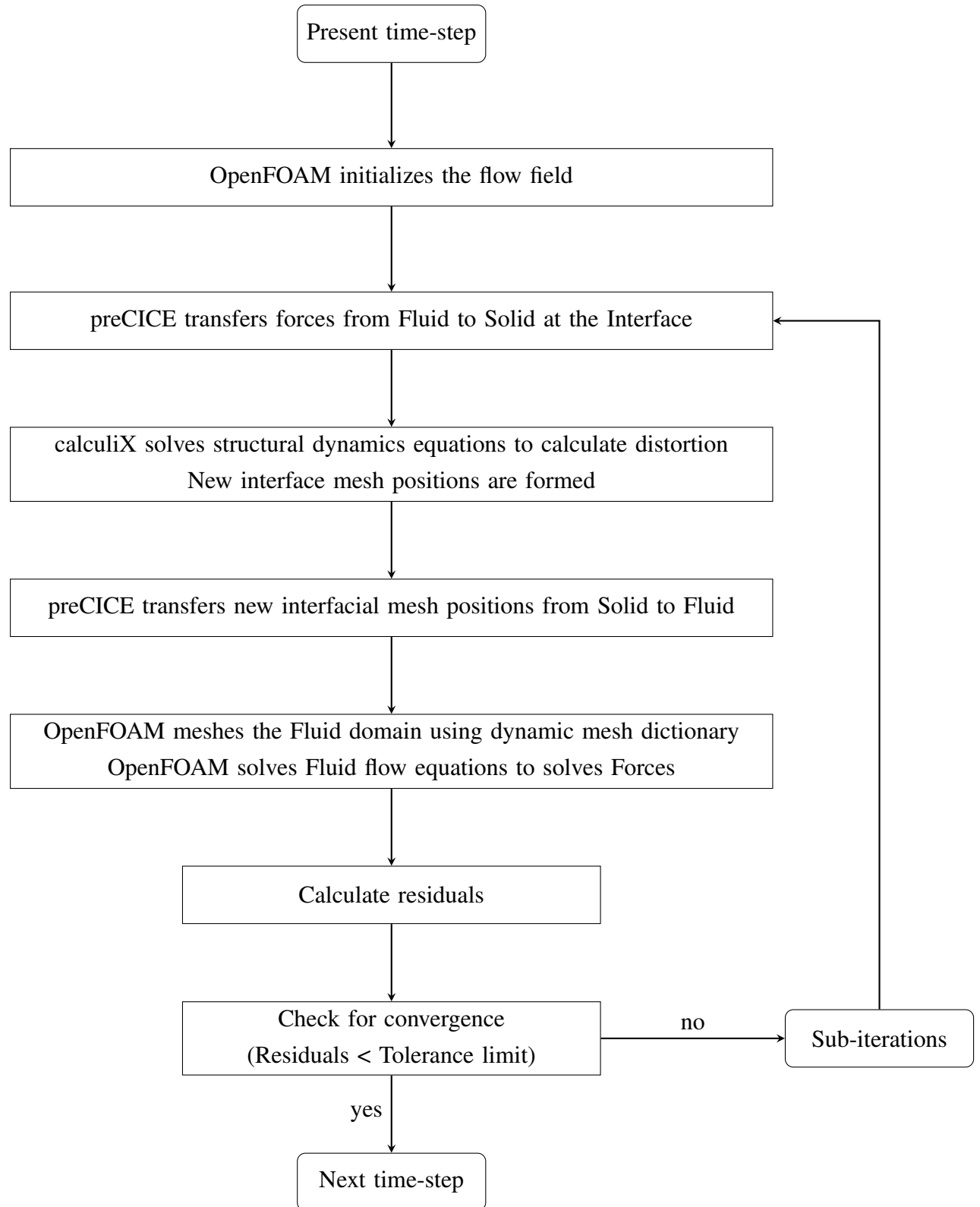
$$E_{ij}^s = \frac{1}{2} \left(\frac{\partial u_i^s}{\partial x_j} + \frac{\partial u_j^s}{\partial x_i} \right) \quad (2.5)$$

Coupling conditions at the interface

To maintain the no-slip condition along the fluid-structure interface, the following Dirichlet and Neumann conditions are imposed [44]

$$u^f = u^s \quad T_{ij}^f n_i = T_{ij}^s n_i$$

2.2 Algorithm



2.3 Overset meshes

2.3.1 Overview

Overset meshing, also known as Chimera or Overlapping meshing is an important development in recent times. Unlike conventional meshes, these consist of at least one subsidiary mesh on another background mesh. The data is interpolated between the subsidiary mesh and the background mesh. Hence, scenarios involving complex motions and moving parts can be easily set up and simulated [45, 46, 47]

2.3.2 Comparison with conventional moving meshes

In the case of overlapping meshes, there exist active and passive cells in the meshes. Active cells are those where the discretizing governing equations are solved, and the passive cells, or ‘hole’ cells are where no equations are solved and they are ignored. Additionally, there are donor and acceptor cells in both the subsidiary and background meshes, where the results of one are interpolated with the other mesh and then the equations are solved in the other and interpolated back into the original mesh. Usually, the external boundary of the subsidiary mesh will have acceptor cells taking in interpolated data from the background mesh. Similarly, the cells of the background mesh near a ‘hole’ in the subsidiary mesh will have acceptor cells, taking in data from the subsidiary mesh. Thus apart from solving the normal discretizing equations in the domain of interest, there is also the extra cost involved when interpolating between cells of both the meshes when using overset or overlapping meshes. Also to reduce numerical errors during interpolation, it is important to have donor cells and acceptor cells to be around the same size. In the figure 2.1, we can see a depiction of the same for a sample mesh that we have used in our study, where the active cells are coloured blue, the interpolating cells (i.e. donor and acceptor cells) are coloured white, and the passive (‘hole’) cells are coloured red.

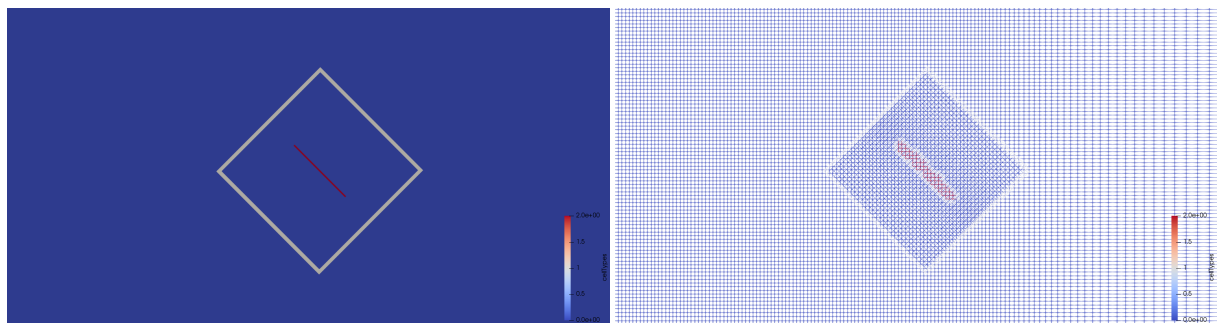


Figure 2.1: Active, Interpolating and Passive cells

In conventional moving meshes, the movement of meshes would be dependent on each other, and if the limit of mesh motion is exceeded the mesh would break and the simulation would not be possible, especially when the amount of displacement is unknown like in a simulation

involving Fluid-Structure Interaction (FSI). Such cases can be easily avoided by creating two independent meshes, and thus overset meshes have an advantage. This also means that we can study the effects of multiple moving bodies at the same time by keeping their motions independent of each other.

Thus, while overset meshes do take up extra computational power, the places where high flexibility and independent movement is required is where overset meshes are useful.

2.4 Fluid solver validation studies using standard test cases

2.4.1 Flow over a circular cylinder

Flow past a stationary circular cylinder is simulated for $Re = 20, 40$ and 100 . The primary motivation behind simulating this test case is to study the alternate shedding of vortices, known as von-Karman vortex shedding formed in the wake region of the cylinder which is a characteristic of unsteady flow over a stationary circular cylinder for Re greater than 47. Procedure to generate structured mesh using blockMesh, visualization techniques using paraFoam, FFT using MATLAB was also learnt in addition to assessing the accuracy of OpenFOAM to simulate uniform flow over a stationary body.

The size of the computational domain is ($-8D \leq x \leq 25D, -8D \leq y \leq 8D$). The center of the cylinder is taken as origin. D is the diameter of the cylinder which is taken as the characteristic length scale for the simulation. The domain is as shown in figure 2.2.

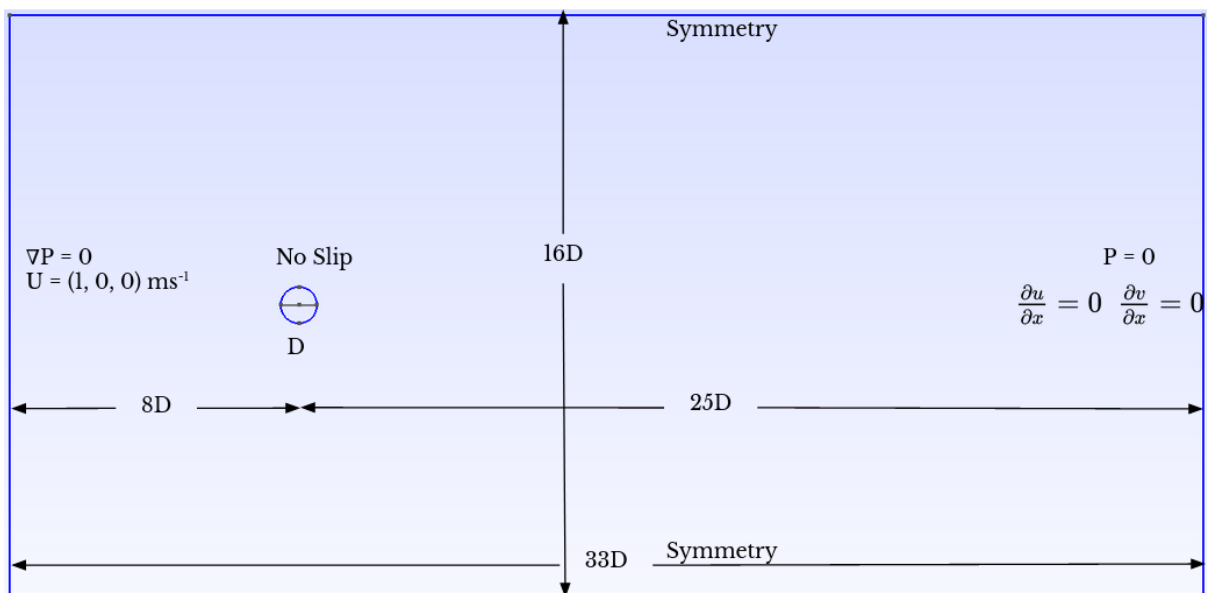
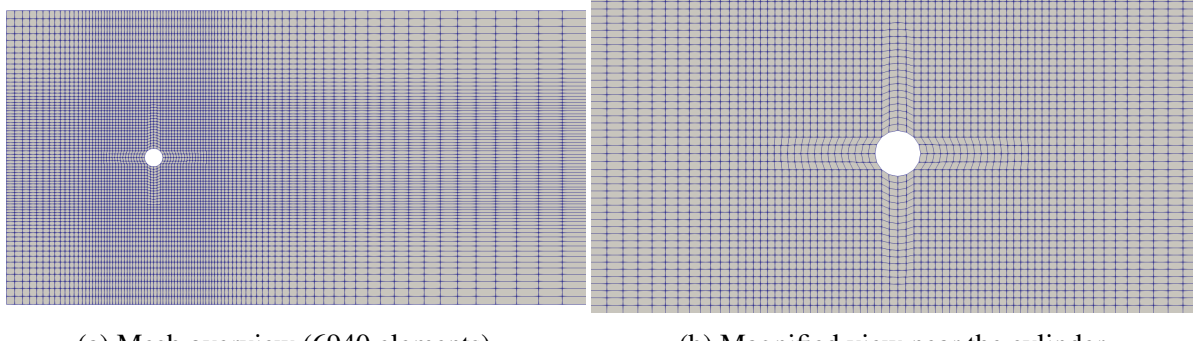


Figure 2.2: Domain for flow over cylinder

The computational domain is discretized into a structured grid of 6940 elements for grade-1 mesh, 15364 elements for grade-2 mesh and 63420 elements for grade-3 mesh. Mesh independency is achieved within these 3 grids. The mesh is generated using blockMesh. The mesh over the whole domain as well as the mesh surrounding the cylinder are shown in figure 2.3



(a) Mesh overview (6940 elements)

(b) Magnified view near the cylinder

Figure 2.3: Mesh for cylinder cases

At the inlet, a Dirichlet condition for velocity is applied by keeping $U_x = 1 \text{ ms}^{-1}$, $U_y = 0$, $U_z = 0$ and a Neumann condition for pressure is applied by keeping $\nabla P = 0$. At the outlet, a Neumann condition for velocity is applied by keeping $\frac{\partial u}{\partial x} = 0$, $\frac{\partial v}{\partial x} = 0$ and a Dirichlet condition for pressure is applied by keeping $P = 0$. A symmetry condition is maintained at the top and bottom. A no-slip condition is maintained on the periphery of the cylinder. The inlet velocity is taken as the characteristic velocity scale. Re is varied by varying kinematic viscosity ν .

The force coefficients for each case are calculated. In addition, Strouhal number was also calculated for the unsteady flow at $Re = 100$. These results are used to quantitatively validate the simulation against standard literature as seen in table 2.1. Even when the mesh is made finer and finer, there is negligible change in results. Hence, mesh independency is achieved. The vorticity plot depicting the alternate shedding for $Re = 100$ is shown in figure 2.4

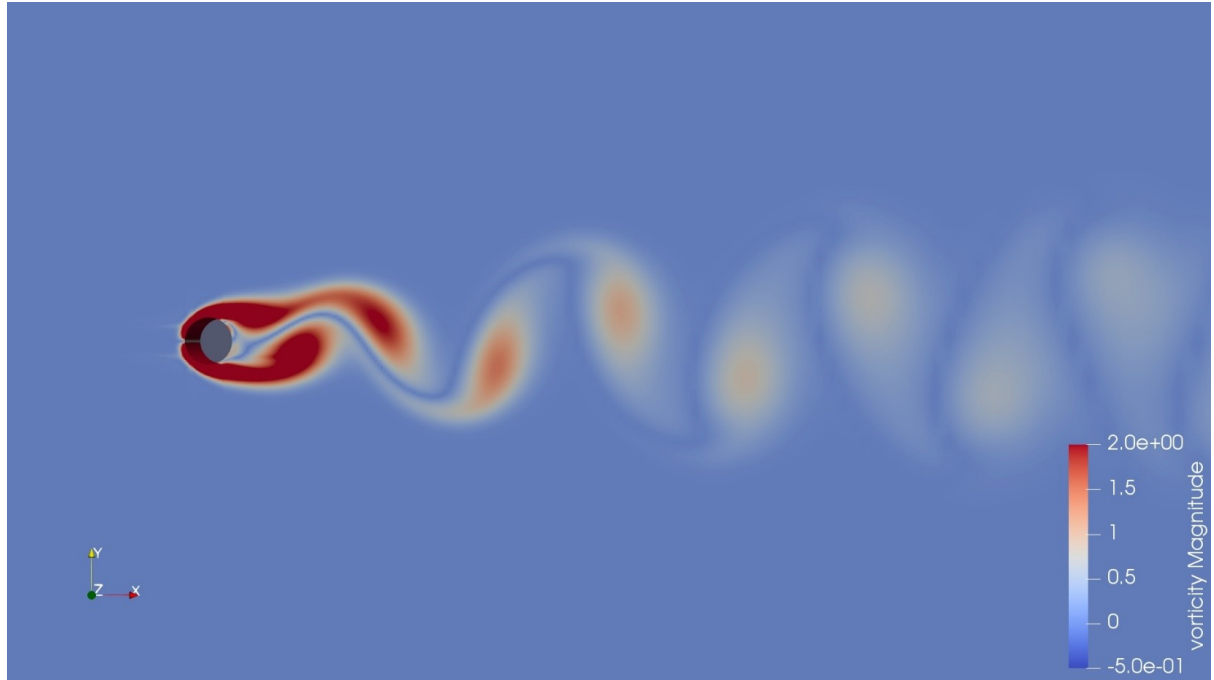


Figure 2.4: Vortex shedding for $Re = 100$

Table 2.1: Quantitative validation of fluid solver with flow over a cylinder test

Re	Author(s)	Method	C_D	St N
$Re = 20$	Coutanceau and Bouard [48]	Experiment	-	-
$Re = 20$	Tritton [49]	Experiment	2.2	-
$Re = 20$	Dennis and Chang [50]	N-S	2.045	-
$Re = 20$	Nieuwstadt and Keller [51]	N-S	2.053	-
$Re = 20$	Hejranfar and Ezzatneshan [52]	CFD-LBM	2.021	-
$Re = 20$	Present work	CFD-OpenFOAM v7	2.24986	-
$Re = 40$	Coutanceau and Bouar [48]	Experiment	-	-
$Re = 40$	Tritton	Experiment [49]	1.65	-
$Re = 40$	Dennis and Chang [50]	N-S	1.522	-
$Re = 40$	Nieuwstadt and Keller [51]	N-S	1.550	-
$Re = 40$	Hejranfar and Ezzatneshan [52]	CFD-LBM	1.515	-
$Re = 40$	Present work	CFD-OpenFOAM v7	1.66477	-
$Re = 100$	Liu et al [53]	N-S	1.35	0.164
$Re = 100$	Calhoun [54]	N-S	1.35	0.175
$Re = 100$	Russell and Wang [55]	N-S	1.38	0.169
$Re = 100$	Chiu et al [56]	N-S	1.35	0.167
$Re = 100$	Hejranfar and Ezzatneshan [56]	CFD-LBM	1.336	0.1626
$Re = 100$	Present work	CFD-OpenFOAM v7	1.37894	0.168

At $Re = 20$ ($\nu = 0.05 \text{ m}^2\text{s}^{-1}$), a zero lift coefficient (C_L) and constant drag coefficient (C_D) are expected which is seen as a time history of force coefficients in figure 2.5

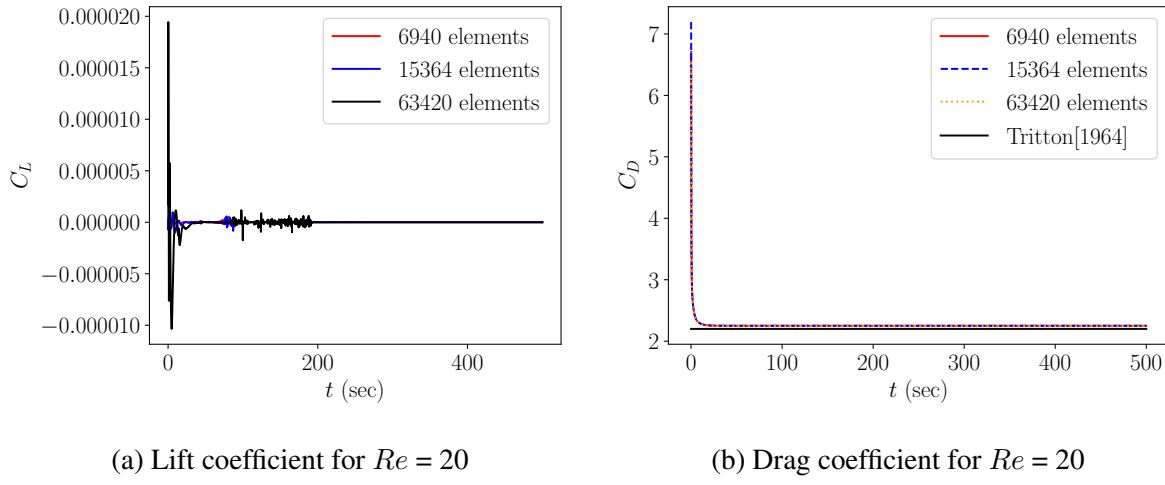
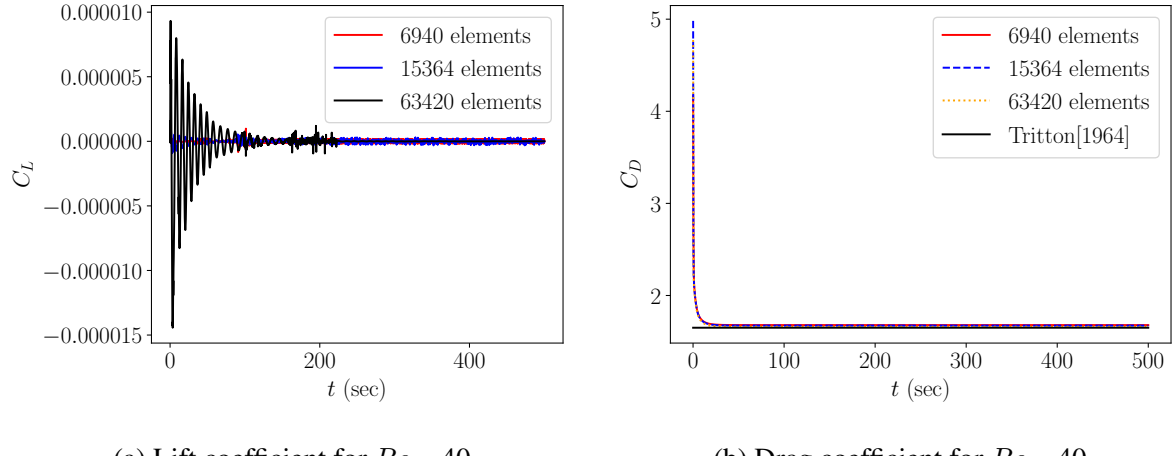


Figure 2.5: Force coefficients for $Re = 20$

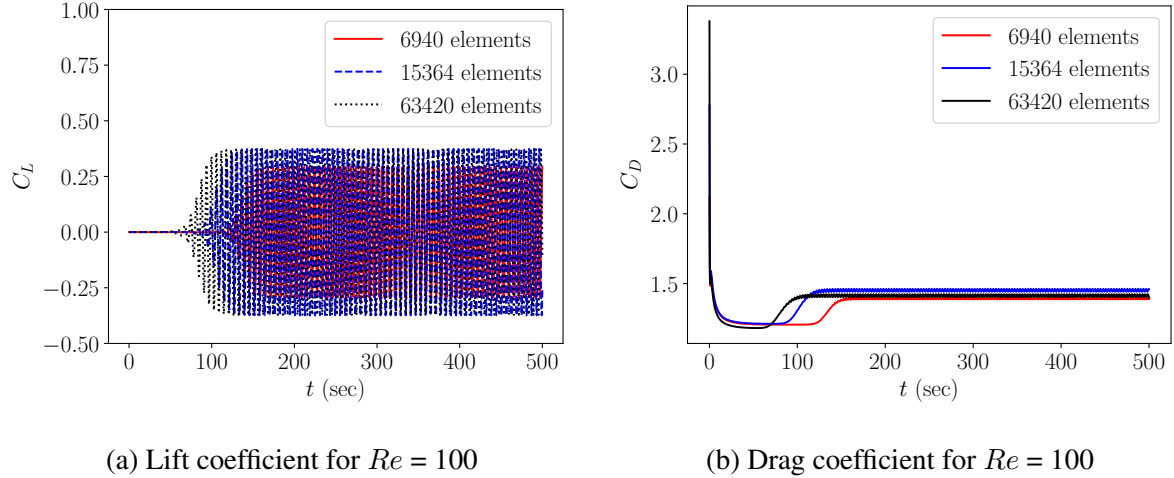
At $Re = 40$ ($\nu = 0.025 \text{ m}^2\text{s}^{-1}$), a zero lift coefficient (C_L) and constant drag coefficient (C_D) are expected which is seen as a time history of force coefficients in figure 2.6



(a) Lift coefficient for $Re = 40$ (b) Drag coefficient for $Re = 40$

Figure 2.6: Force coefficients for $Re = 40$

At $Re = 100$ ($\nu = 0.01 \text{ m}^2\text{s}^{-1}$), an oscillating lift coefficient (C_L) and time-varying drag coefficient (C_D) are expected which is seen a time history of force coefficients in figure 2.7.



(a) Lift coefficient for $Re = 100$

(b) Drag coefficient for $Re = 100$

Figure 2.7: Force coefficients for $Re = 100$

2.4.2 Laminar flow around an airfoil

An airfoil, because of its complex shape, is hard to model in some solvers. In order to get good accuracy, while keeping computational load small, we need to grade the mesh from close to the airfoil towards the edge of the boundaries. Since it is complicated to construct a structured mesh for the airfoil, we have to construct unstructured meshes for the same. Here, we present a standard case to verify the unstructured mesh that we use, as we will be working with airfoils in further studies. Here, we used open source software *gmsh* to generate the unstructured mesh and carried out simulations using OpenFOAM 7.

The size of the computational domain is ($-7.57c \leq x \leq 25.43c$, $-8.25c \leq y \leq 7.75c$). The leading-edge of the airfoil is taken as origin. c is the chord length of the airfoil NACA 0012 airfoil which is taken as the characteristic length scale for the simulation. The domain is as shown in figure 2.8.

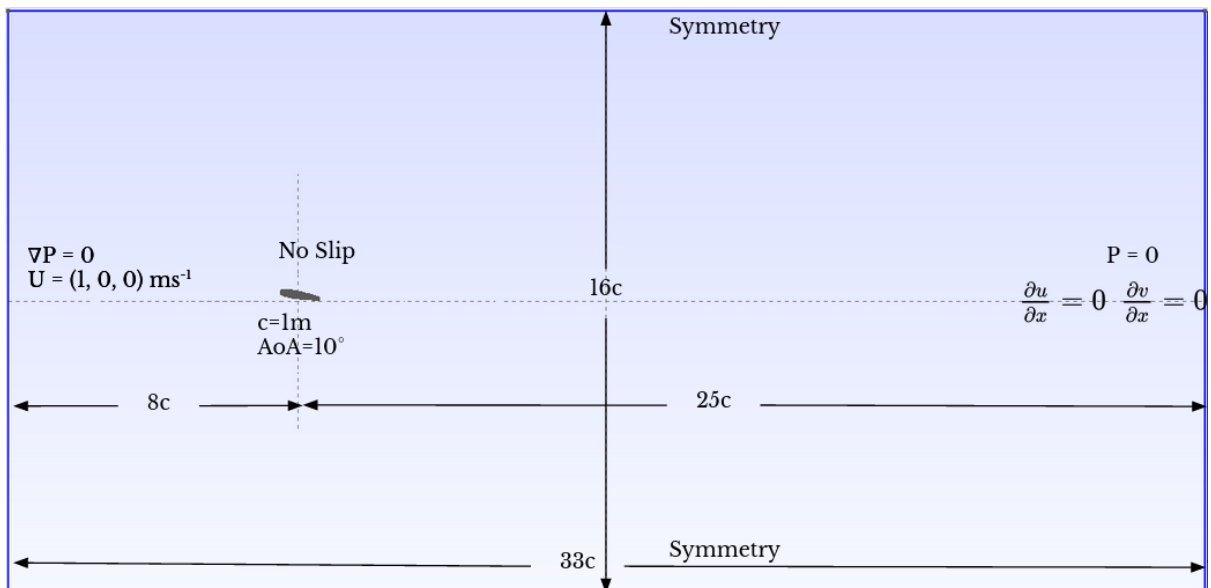


Figure 2.8: Domain used for laminar flow over an airfoil

The computational domain is discretized into a structured grid of 83214 elements for grade-1 mesh, 328766 elements for grade-2 mesh. Mesh independency is achieved within these 2 grids. The mesh over the whole domain as well as the finer mesh surrounding the airfoil are shown in figure 2.9

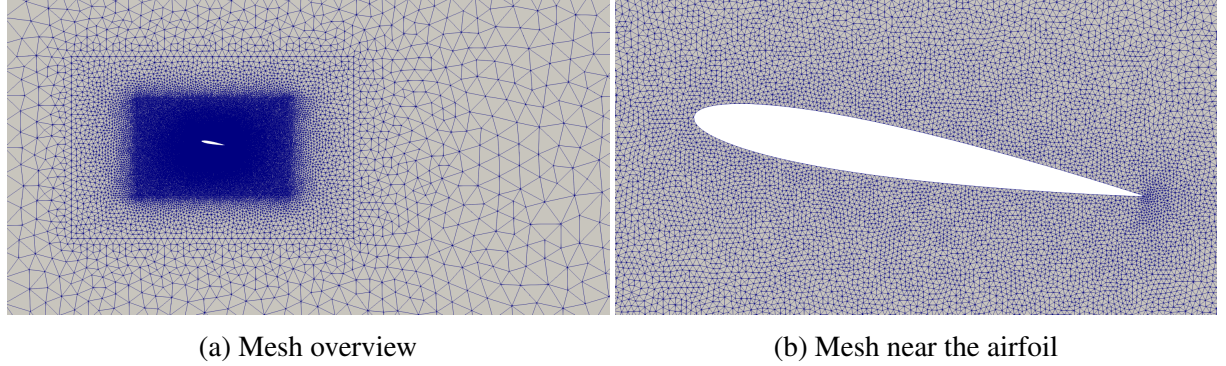


Figure 2.9: Visualization of the mesh

In this case the angle of attack is maintained at 10^0 , while Reynolds number(Re) of the flow is 1000. At the inlet, there is a constant velocity of 1 in the x-direction, while the rest of the velocity components are 0, and a Neumann condition for pressure is applied by keeping $\nabla P = 0$. At the outlet, a Neumann condition for velocity is applied by keeping $\frac{\partial u}{\partial x} = 0, \frac{\partial v}{\partial x} = 0$ and a Dirichlet condition for pressure is applied by keeping $P = 0$. A symmetry condition is maintained at the top and bottom. A no-slip condition is maintained on the periphery of the airfoil. The inlet velocity of 1 is taken as the characteristic velocity scale.

The force coefficients are calculated. After a certain time, one can see oscillations in the force coefficients due to vortex shedding. The force coefficients calculated are compared with and plotted against literature, Zhe Fang, 2019[54] in figure 2.10. Even when the mesh is made finer and finer, there is negligible change in results. Hence, mesh independency is achieved. The minor over-prediction in case of C_l might be attributed to the fact that in Zhe Fang, 2019[54], Lattice-Boltzmann method was implemented was used to solve fluid flow equations and we have employed a finite volume method.

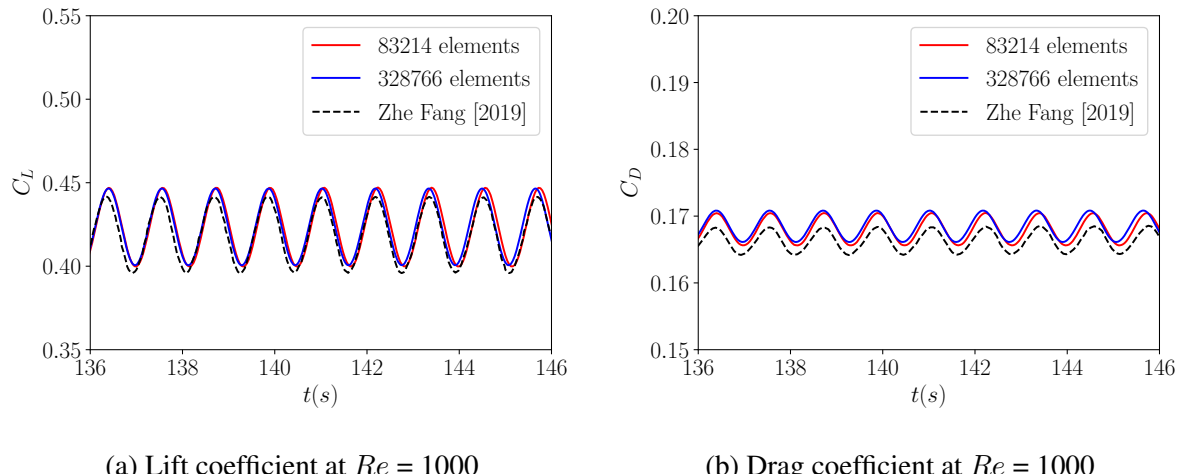


Figure 2.10: Comparison of force coefficients for laminar flow over the airfoil at $Re = 1000$

2.4.3 Accelerating airfoil

Translational acceleration is an important phase in insect flight. To validate the accuracy of the fluid solver involving accelerating bodies, a NACA 0012 airfoil at an angle of attack 35^0 is simulated. Similar to the previous case, *gmsh* was used to generate the mesh used to validate the accuracy of OpenFOAM 7 to simulate an accelerating body.

The size of the computational domain is ($-7.57c \leq x \leq 25.43c$, $-8.25c \leq y \leq 7.75c$). The leading-edge of the airfoil is taken as origin. c is the chord length of the airfoil NACA 0012 airfoil which is taken as the characteristic length scale for the simulation. The domain is as shown in figure 2.11.

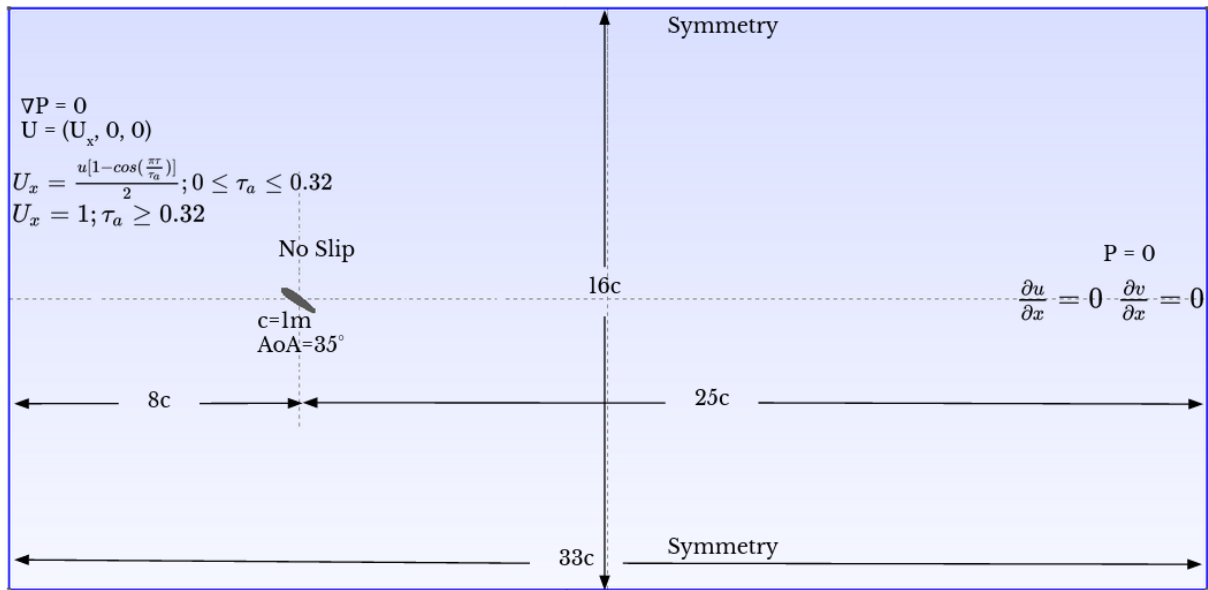


Figure 2.11: Domain used for accelerated airfoil

The computational domain is discretized into a structured grid of 83452 elements for grade-1 mesh, 328260 elements for grade-2 mesh and 449728 elements for grade-3 mesh. Mesh independency is achieved within these 3 grids.

The airfoil is accelerated from rest for a non-dimensional time $\tau_a = 0.32$, to reach a constant non-dimensional velocity $u = 1$. This is done by giving boundary conditions at the inlet, as

$$\begin{aligned} U_x &= u[1-\cos(\pi \tau/\tau_a)]/2 && \text{for } 0 \leq \tau \leq 0.32 \\ U_x &= 1 && \text{for } \tau > 0.32 \end{aligned}$$

$U_y = 0$, $U_z = 0$ and a Neumann condition for pressure is applied by keeping $\nabla P = 0$. At the outlet, a Neumann condition for velocity is applied by keeping $\frac{\partial u}{\partial x} = 0$, $\frac{\partial v}{\partial x} = 0$ and a Dirichlet condition for pressure is applied by keeping $P = 0$. A symmetry condition is maintained at the top and bottom. A no-slip condition is maintained on the periphery of the airfoil. The inlet velocity u is taken as the characteristic velocity scale.

The force coefficients are calculated. As expected, we see a spike in the forces during the acceleration phase. This acceleration has an effect on the flight characteristics until 7 chord lengths are traversed after which steady state force values are obtained. These results are used to quantitatively validate the simulation against standard literature as seen in figure 2.12. The error in C_L maybe attributed to the fact that Hamdani (2000) [57] used a compressible solver to solve incompressible flow at Mach number 0.1, while in present work an incompressible solver is utilized. Even when the mesh is made finer and finer, there is negligible change in results. Hence, mesh independency is achieved. The vorticity plot depicting the vortex shedding is shown in figure 2.13 where it is also qualitatively validated against vorticity plots from Hamdani (2000) [57]

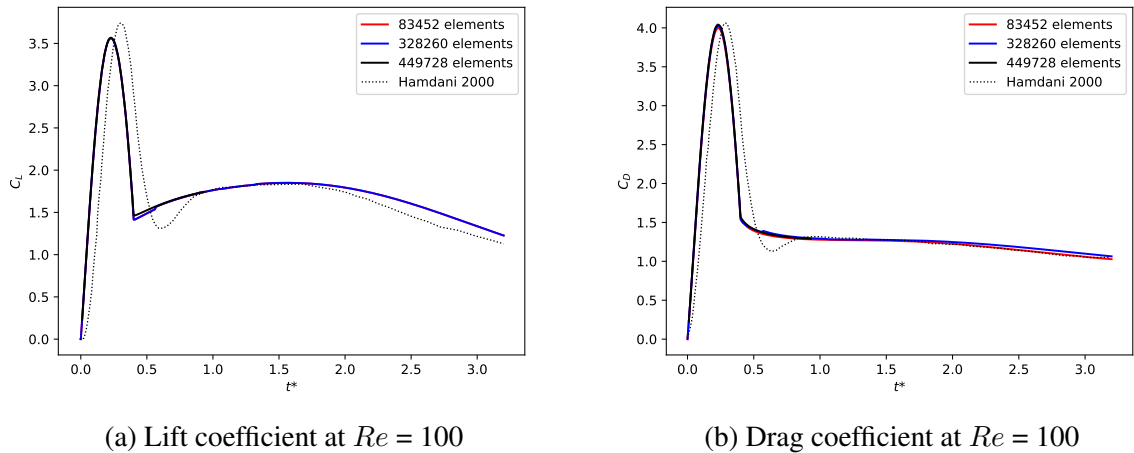


Figure 2.12: Comparison of force coefficients for accelerating airfoil at $Re=100$

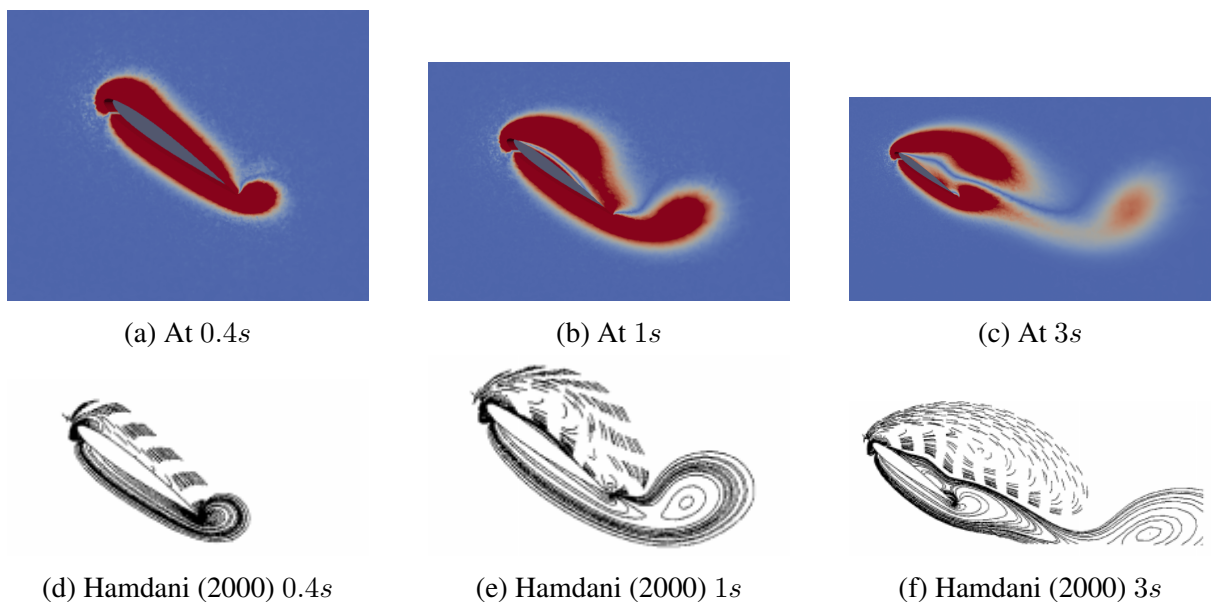


Figure 2.13: Vorticity and comparison with Hamdani(2000)

2.5 Structural dynamics solver validation studies using standard test cases

2.5.1 Small deflection of a cantilever beam

A cantilever beam under a tip load is simulated using CalculiX. The primary motivation behind simulating this test case is to evaluate the accuracy of CalculiX to solve linear structural dynamics equations. In order to do that, procedure to generate structured mesh, giving boundary conditions using cgx, visualization, post-processing techniques using cgx, was also learnt in addition to validating the accuracy of Calculix to simulate small deflection of a cantilever beam.

The length of the beam is 8 m, height 1 m and thickness 1 m. The beam is oriented such that the length is along the x-axis, height along the y-axis, thickness along the z-axis. The elastic modulus of the isotropic beam is 210 GPa and its Poisson's ratio is 0.3.

The beam is discretized into 32 elements (8 along length, 2 along height and 2 along thickness). The elements used here are linear 8 noded brick elements (he8). One end of the beam is fixed by arresting the corresponding nodes in space, constraining all their degrees of freedom. At the free end of the beam, the nodes are not allowed to move in the z-direction. On the free end of the beam, a tip load of 9 MN is acted along y-axis. The case description is as shown in figure 2.14.

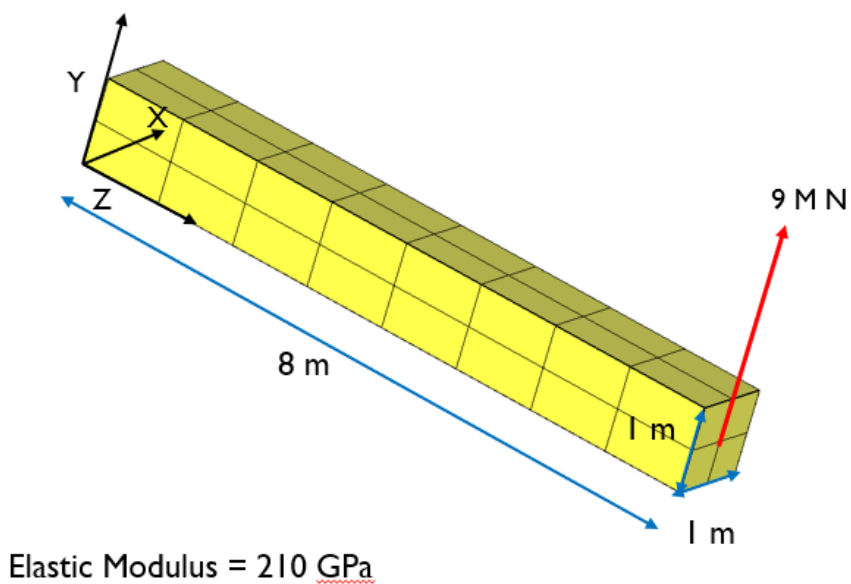


Figure 2.14: Small deflection of a cantilever beam

The vertical displacement of the tip of the free end of the beam is taken as our result and is quantitatively validated against the theoretical value of the displacement obtained by using Euler-Bernoulli beam theory which is given by

$$\delta = \frac{FL^3}{3EI}$$

where F is the applied load, L is the length of the beam, E is the Elastic Modulus and I is the Area Moment of Inertia. The agreement with theoretical value can be seen in table 2.2

Table 2.2: Quantitative validation of solid solver with small deflection of a cantilever beam

Technique	Displacement of the tip along the Y-axis
present work	87.6 mm
Euler-Bernoulli beam theory	87.8 mm

2.5.2 Large deflection of a cantilever beam involving geometric non-linearity

Insect wings undergo large deflection during the rotational phase of their flapping motion. Hence it was necessary to validate the accuracy of the structural dynamics solver in simulating a case involving large deflection. Large deformations in structures lead to geometric non-linearity in which the displacement-strain relationship becomes non-linear. This is not to be confused with material non-linearity which occurs due to a non-linear stress-strain relationship. The primary motivation behind simulating this test case is to evaluate the accuracy of CalculiX to solve non-linear structural dynamics equations. In order to do that, procedure to generate structured mesh with reduced quadratic beam elements, giving boundary conditions using cgx, visualization, post-processing techniques using cgx, was also learnt in addition to validating the accuracy of Calculix to simulate large deflection of a cantilever beam.

The length of the beam is 10 m, height 147.8 mm and thickness 100 m. The beam is oriented such that the length is along the x-axis, height along the y-axis, thickness along the z-axis. The elastic modulus of the isotropic beam is 100 MPa and its Poisson's ratio is 0.

The beam is discretized into 40 elements (10 along length, 2 along height and 2 along thickness). Initially, linear 8 noded brick elements (he8) were used which lead to inaccurate prediction of displacements. This might be due to shear locking. To correct this, reduced-integration 20 noded quadratic brick elements (he20r) were used. One end of the beam is fixed by arresting the corresponding nodes in space, constraining all their degrees of freedom. At the free end of the beam, the nodes are not allowed to move in the z-direction. On the free end of the beam, a tip load of 269.35 N is applied along y-axis. The case description is as shown in figure 2.15.

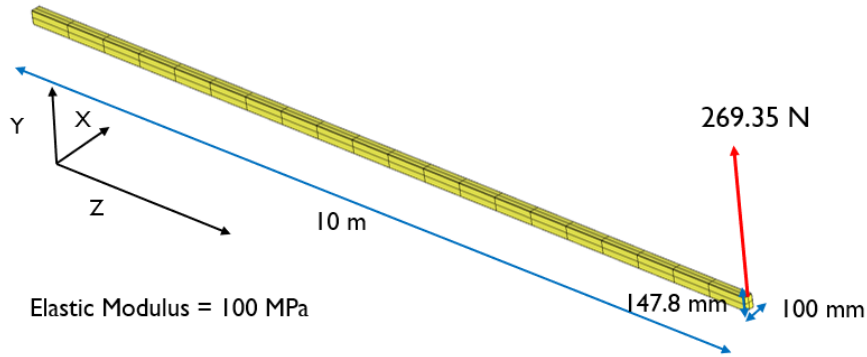


Figure 2.15: Large deflection of a cantilever beam

The tip of the beam is initially under a very small load. It is brought under a final load of 269.35 N after uniformly incrementing the applied force. The displacement of the tip of the beam is plotted at every increment and shown as a displacement history of the tip which is compared with exact solution for the inextensible beam, as given by Bisschopp and Drucker (1945) [58] is shown in figure 2.16. The displacement of the tip in both horizontal and vertical directions is quantitatively validated with the exact solution in table 2.3

Table 2.3: Quantitative validation of solid solver with large-deflection of a cantilever beam

Technique	Horizontal displacement	Vertical displacement
present work	-5.554912 m	8.110299 m
Bisschopp and Drucker (1945) [58]	-	8.123499 m

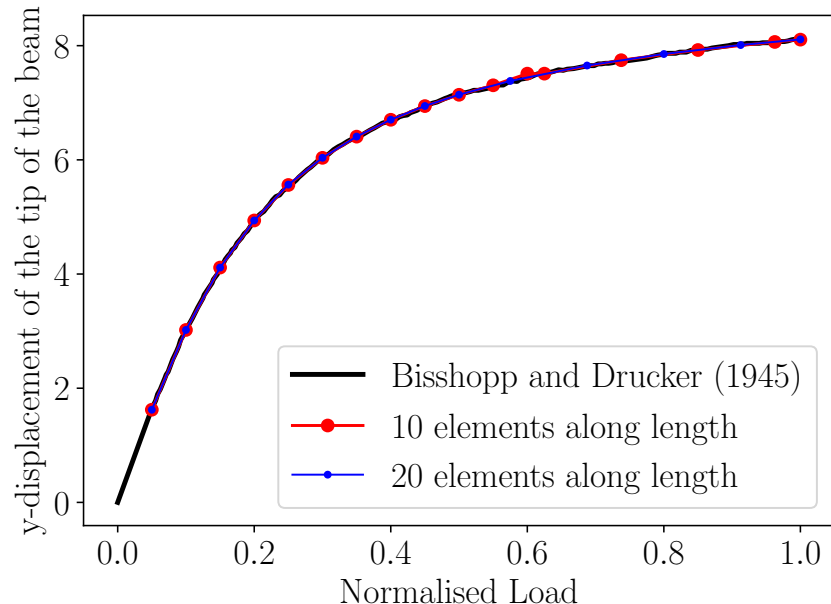


Figure 2.16: Comparison of displacement history of the tip

2.6 Coupling library validation studies using standard test cases

After both the fluid solver (OpenFOAM) and structural dynamics solver (CalculiX) have been validated with respective test cases, they were coupled with the open-source coupling library preCICE. Before insect flight studies are performed it is customary to quantitatively validate the accuracy of the coupling library to conduct Fluid-structure interaction simulations.

2.6.1 Lid-driven cavity with elastic bottom

Laminar flow inside a two-dimensional square cavity consisting of an elastic bottom is simulated. The primary motivation behind simulating this popular fluid-structure interaction benchmark is to study the deformation of an elastic body suspended in a fluid flow dominated by the convective effects. In addition to building a set-up to conduct fluid-structure interaction simulations, and validating the accuracy of the coupling set-up to simulate FSI simulations, the procedure to implement user-defined non-standard boundary conditions in OpenFOAM using a third party library named groovyBC was explored. The same is utilized for all the following studies and it is bench-marked using this case as well.

The size of the computational domain for the fluid regime is ($0 \leq x \leq 1$ m; $0 \leq y \leq 1$ m). The bottom-left corner of the square cavity is taken as origin. The region in ($x = 0$; $0.875 \text{ m} \leq y \leq 1 \text{ m}$) is considered inlet. The region in ($x = 1 \text{ m}$; $0.875 \text{ m} \leq y \leq 1 \text{ m}$) is considered outlet. The region in ($0 \leq x \leq 1 \text{ m}$; $y = 1 \text{ m}$) is considered as a moving wall. The boundary regions in ($x = 0$; $0 \leq y \leq 0.875 \text{ m}$) and ($x = 1 \text{ m}$; $0 \leq y \leq 0.875 \text{ m}$) are considered fixed walls. Agreement with the benchmark results is achieved when the square shaped fluid domain is discretized by a structured grid of 32*32 cells. Additionally the domain is discretized by a structured grid of 24*24, 40*40 cells, 48*48 cells, and 64*64 cells in order to achieve grid independence. The domain is as shown in figure 2.17.

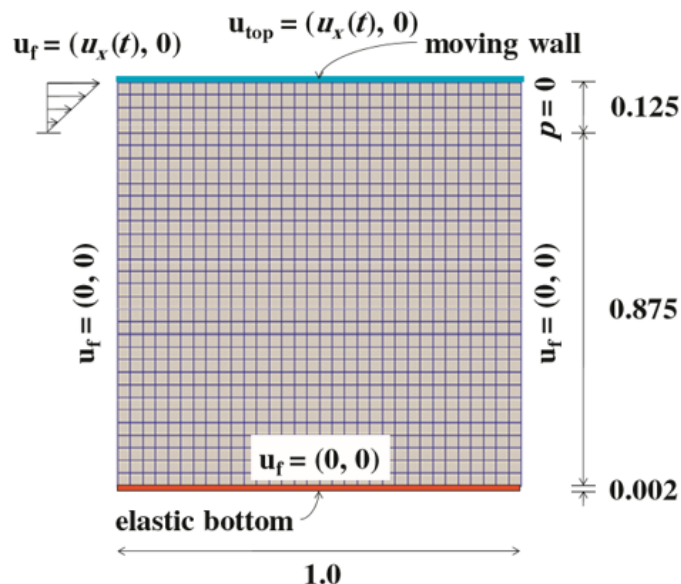


Figure 2.17: Domain for Lid-driven cavity with elastic bottom

On the top wall, horizontal velocity oscillating between 0 and 2 ms^{-1} is given by

$$U_x = 1 - \cos(2\pi t/5); \quad U_y = 0; \quad U_z = 0$$

On the inlet, a linear horizontal velocity profile which oscillates between 0 and 2 is given by

$$U_x = (y - 0.875)(1 - \cos(2\pi t/5)); \quad U_y = 0; \quad U_z = 0$$

On the fixed walls and the bottom, a no-slip condition for velocity and a Neumann condition for pressure is applied by maintaining $\nabla P = 0$. On the outlet $\frac{\partial u}{\partial x} = 0$ and $\frac{\partial v}{\partial x} = 0$ is applied and a Dirichlet condition for pressure is applied by maintaining $P = 0$.

The size of the computational domain for the solid is ($0 \leq x \leq 1 \text{ m}$; $-0.002 \text{ m} \leq y \leq 0$). The elastic bottom is of length 1m and height 0.002 m. The beam is oriented such that the length is along the x-axis, height along the y-axis. The elastic modulus of the isotropic beam is 250 Pa, its Poisson's ratio is 0 and its density is 500 kg m^{-3} . The beam shaped solid domain is discretized by a structured grid of $32*1$ cells, and correspondingly, $24*1$, $40*1$, $48*1$, and $64*1$ cells corresponding to the number of cells used in fluid domain. The elements used here are reduced-integration 20 noded quadratic brick elements (he20r). Both ends of the beam ($x = 0$ and $x = 1 \text{ m}$) are fixed by arresting the corresponding nodes in space, constraining all their degrees of freedom. Translation along z-axis is restrained for nodes all throughout the beam.

The vortex generated due to fluid flow at the top of the cavity generates forces that cause a deflection in the elastic bottom. Vorticity plots at various instances for $24*24$ grid is shown in figure 2.18.

The resulting y -deflection of the center of the beam is compared with standard literature, and plotted against it as shown in figure 2.19 [59]. This also shows achievement of mesh-independency in using the FSI solver.

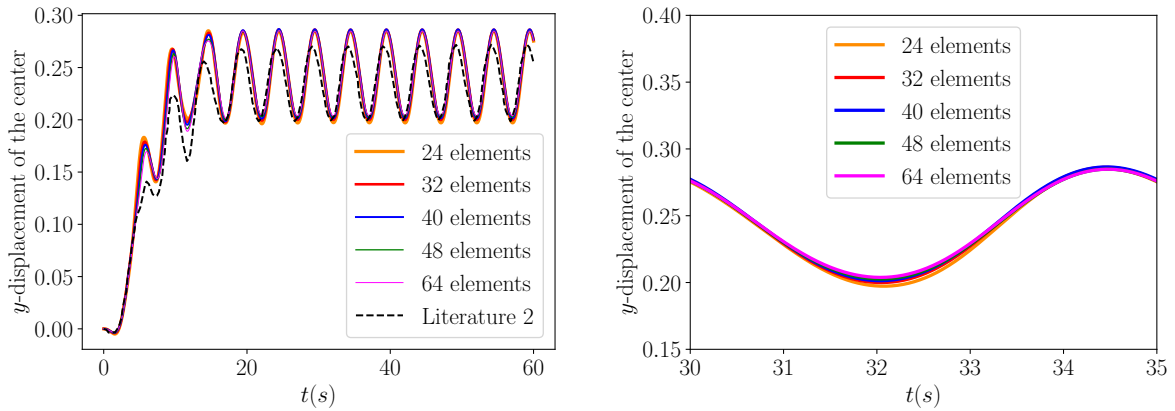


Figure 2.19: Comparison of deflection of the center of the elastic flap

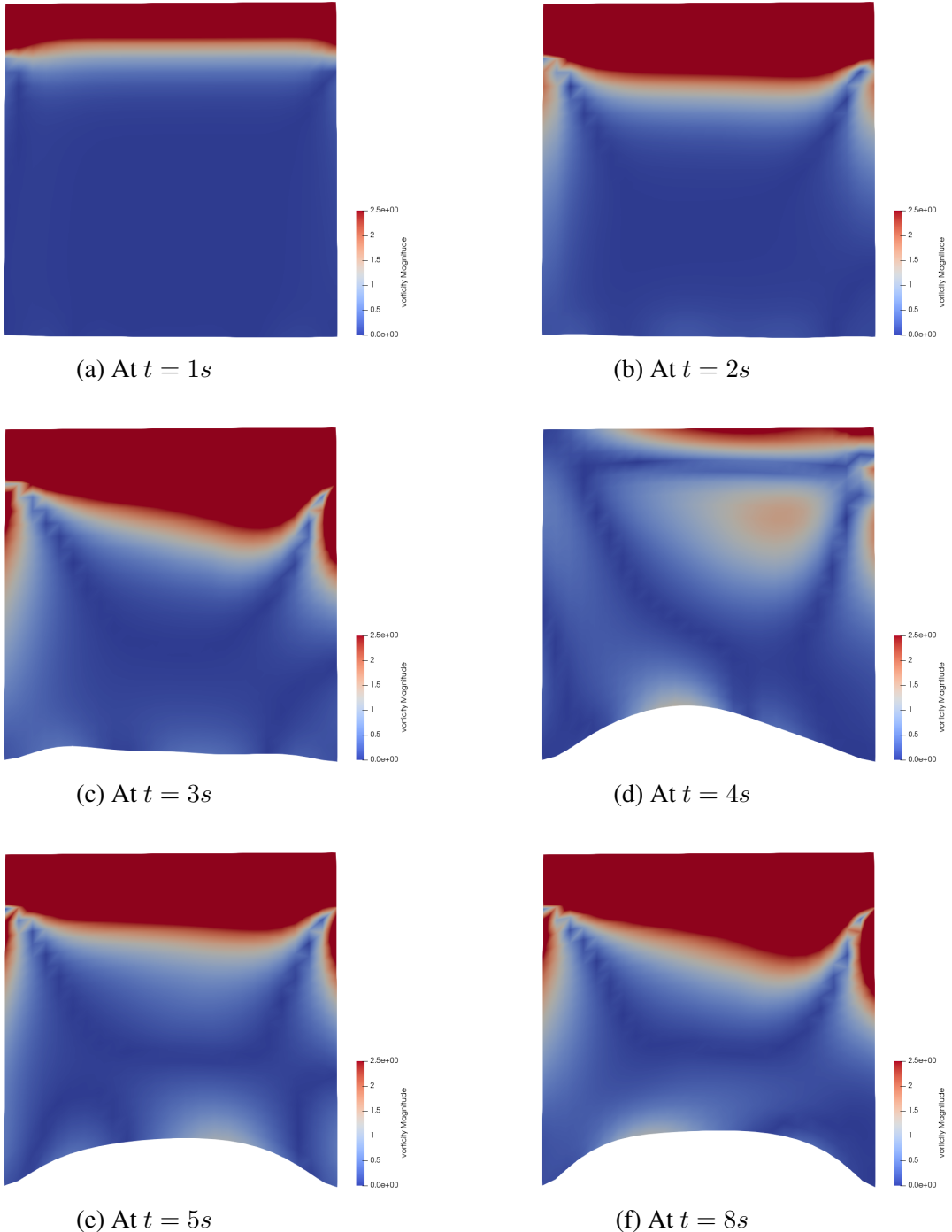


Figure 2.18: Vorticity plots for Lid-driven Cavity with elastic bottom at various instances

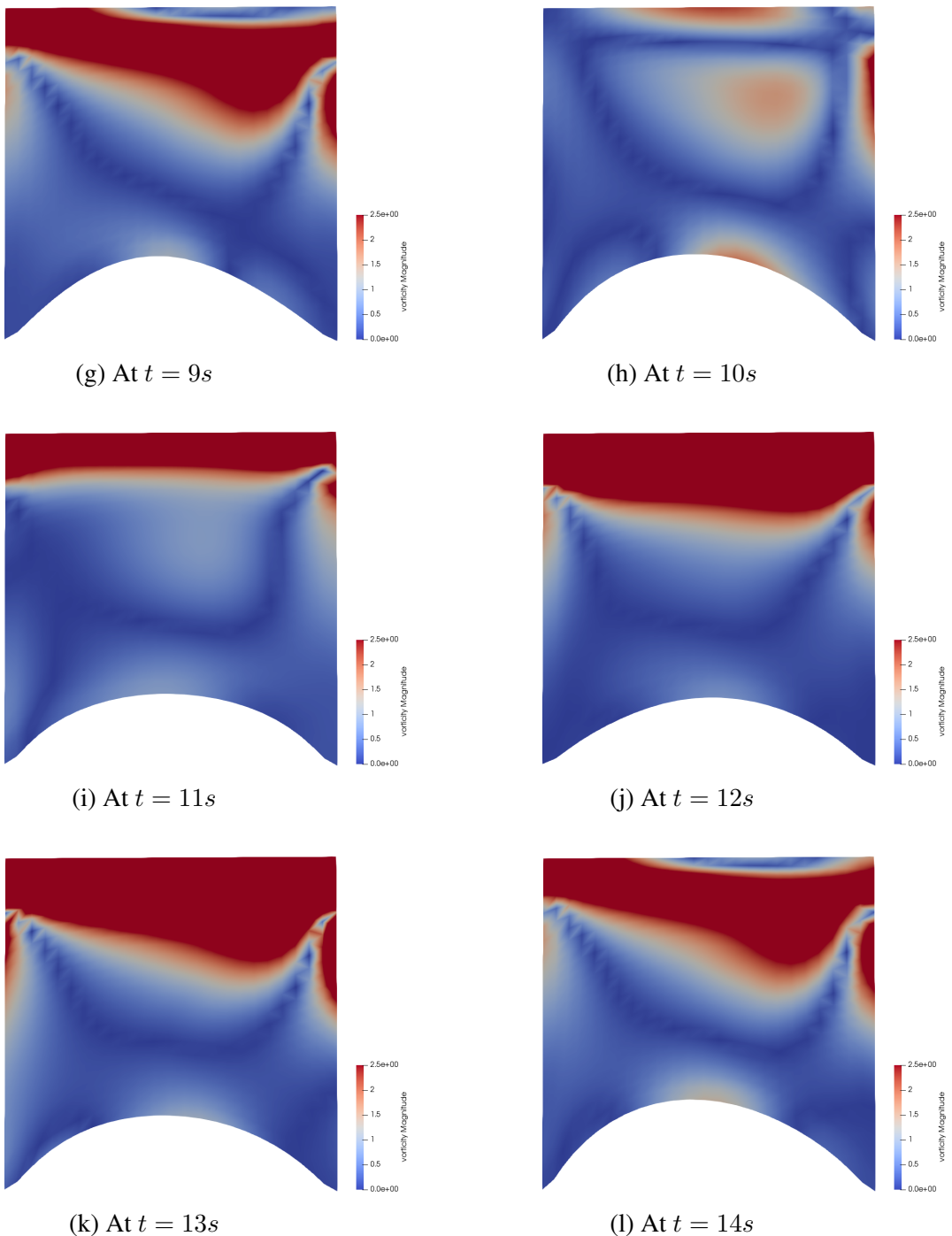


Figure 2.18: Vorticity plots for Lid-driven Cavity with elastic bottom at various instances (cont)

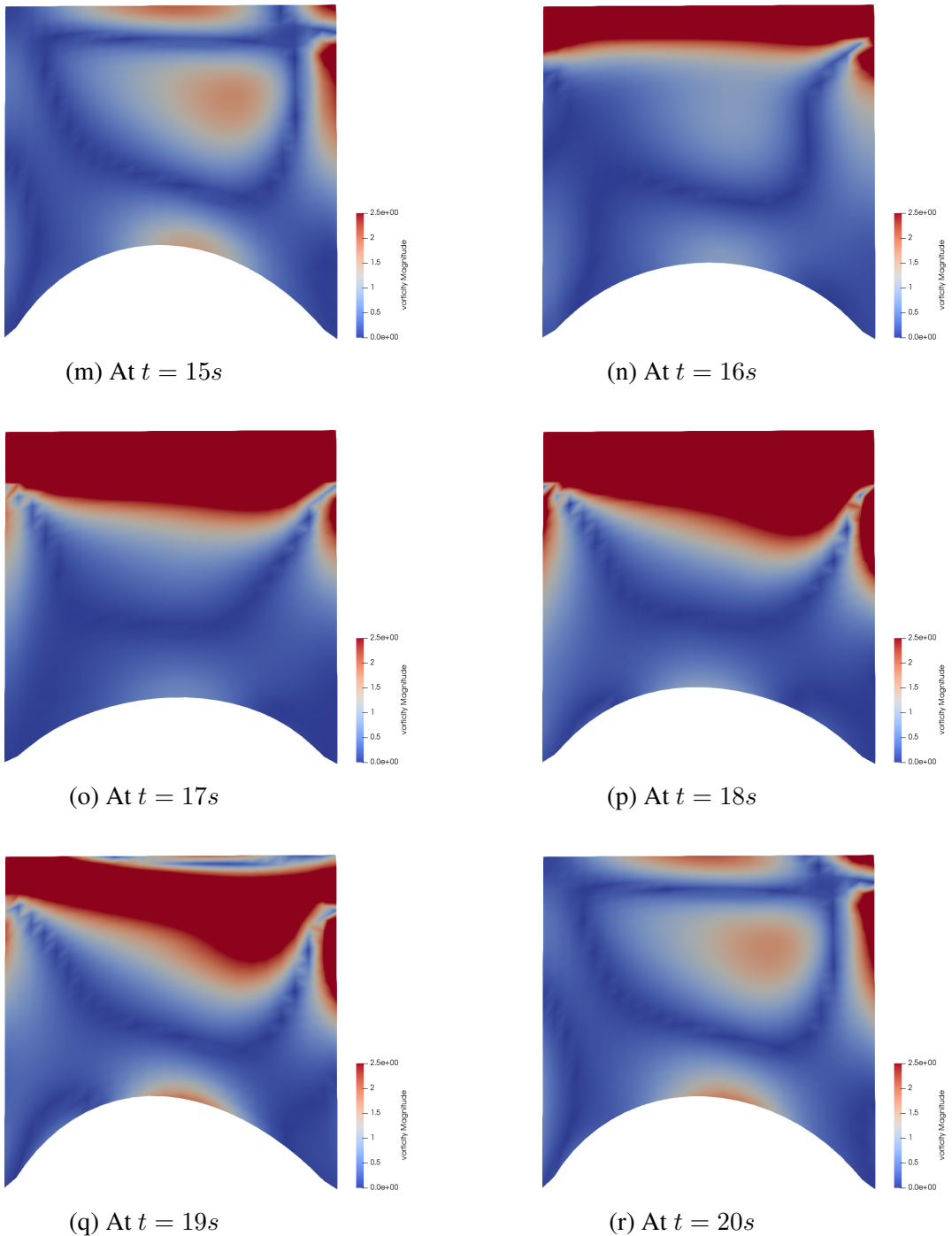


Figure 2.18: Vorticity plots for Lid-driven Cavity with elastic bottom at various instances (cont)

While trying to achieve grid-independence for this case, the simulation was diverging when the square domain was divided finer than 48x48 cells. Upon tinkering and several tries later, the problem was pinpointed to be arisen due to the choice of surface normal gradient scheme. According to OpenFOAM User Guide [41], the choice of surface normal gradient scheme is important because they are required to evaluate a Laplacian term using Gaussian integration. A surface normal gradient is evaluated at a cell face; it is the component, normal to the face, of the gradient of values at the centres of the 2 cells that the face connects.

As enquiring the reason behind the effect of the choice of surface normal gradient schemes on the numerical simulation doesn't come under the scope of this thesis, the results produced in the divergent simulations for this particular case are provided in fig 2.20

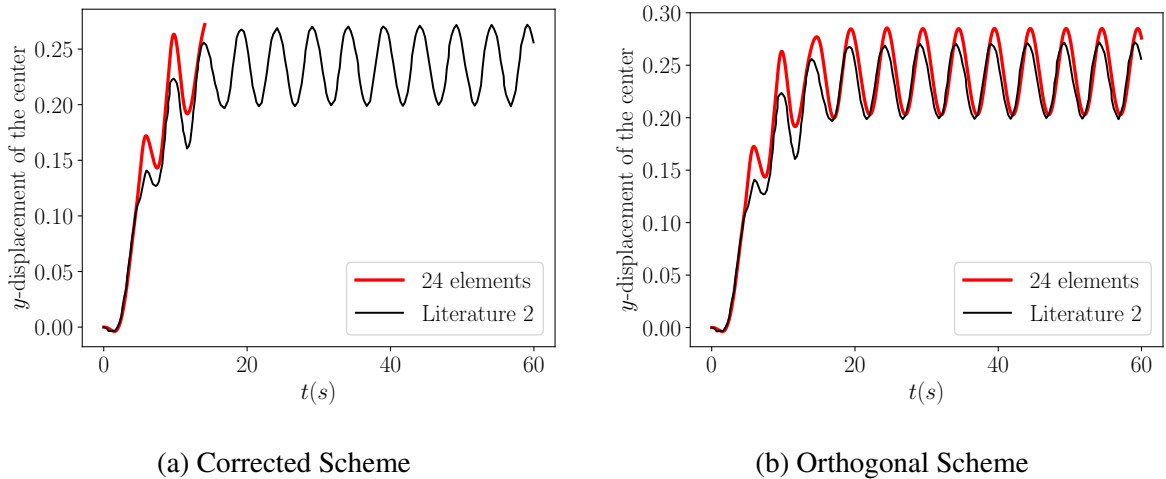


Figure 2.20: Depiction of effect of Surface Normal Gradient Scheme on Numerical Stability

2.6.2 Elastic cantilever attached to a circular bluff body

This case combines two cases discussed in the earlier sections namely, *Flow over a circular cylinder* and *Large deflection of a cantilever beam involving geometric non-linearity*. We try to benchmark the deflection of a cantilever beam attached to the wake region of a cylinder over which an incompressible laminar flow is projected inside a channel. If the motion of the elastic body suspended in the fluid flow is dominated by the convective effects in the earlier case *Lid-driven cavity with elastic bottom*, this case represents a fluid-structure interaction example in which the vortex excited elastic body motion is studied and the accuracy of the computational model is validated.

The size of the computational domain for the fluid regime, that is the channel is given by ($0 \leq x \leq 2.5$ m; $0 \leq y \leq 0.41$ m). The bottom-left corner of the channel is taken as origin. The center of the cylinder is at (0.2,0.2). D is the diameter of the cylinder which is taken as

the characteristic length scale for the simulation. The results were presented for $D = 1\text{ m}$. A cantilever of length 0.350m and height 0.02m is attached to the cylinder. The region covered by the cantilever is given by $(0.25 \leq x \leq 0.6\text{ m}; 0.19 \leq y \leq 0.21\text{ m})$. The domain is as shown in figure 2.21 [60].



Figure 2.21: Domain for Elastic cantilever attached to a circular bluff body

At the inlet, a parabolic velocity profile is applied by giving

$$U_x = 1.5Uy(H-y)/(H/2)^2; \quad U_y = 0; \quad U_z = 0$$

A Neumann condition for pressure is applied by keeping $\nabla P = 0$. At the outlet, we have $\frac{\partial u}{\partial x} = 0$, $\frac{\partial v}{\partial x} = 0$ and a Dirichlet condition for pressure is applied by keeping $P = 0$. A no-slip condition is maintained on the periphery of the cylinder, on the periphery of the cantilever, top and bottom of the channel.

The cantilever is discretized into 40 elements (10 along length, 1 along height and 1 along thickness). The elements used here are reduced-integration quadratic beam elements (he20r). One end of the beam ($x = 0.6\text{ m}; 0.19 \leq y \leq 0.21\text{ m}$) is fixed by arresting the corresponding nodes in space, constraining all their degrees of freedom. At the free end of the beam ($x = 0.6\text{ m}; 0.19 \leq y \leq 0.21\text{ m}$), the nodes are not allowed to move in the z-direction. Rotation along all the axes is restrained for nodes all throughout the beam.

This specific Fluid-structure Interaction case is further sub-divided into 3 sub-cases dictated by 3 non-dimensional numbers given in table 2.4. The symbols used for this particular case and their meaning is given in table 2.5. As it can be seen in table 2.4, the ratio of the densities of solid and fluid are in the order 1 to 10^1 which is meaningful to the case of insect flight. In addition to that, ratio of the densities of solid and fluid greatly affects the numerical stability of an FSI problem.

Table 2.4: Non-dimensional parameters

Parameter	FSI1	FSI2	FSI3
$\beta = \rho^s/\rho^f$	1	10	1
ν^s	0.4	0.4	0.4
$A_e = E^s/(\rho^f U^2)$	3.5×10^4	1.4×10^3	1.4×10^3

Table 2.5: Symbols for Elastic cantilever attached to a circular bluff body

Symbol	Parameter
ρ^s	Density of the solid flap
ν^s	Poisson's ratio of the solid flap
ρ^f	Density of the Fluid
ν^f	Kinematic Viscosity of the Fluid
U	Characteristic Velocity scale

Since the parameter, β ratio of the densities of solid and fluid greatly influences the numerical stability of an FSI problem, it is important to mention the selection of ρ^s , the density of solid and ρ^f , the density of fluid along with every FSI study.

FSI1

In this particular case, flow is described by $Re = 20$. As a characteristic of that flow around that Re , there's a constant lift force generated in the wake region of the cylinder as a result of a steady state. This constant lift force acts on the lower surface of the cantilever beam resulting in a constant deflection at every point of the beam.

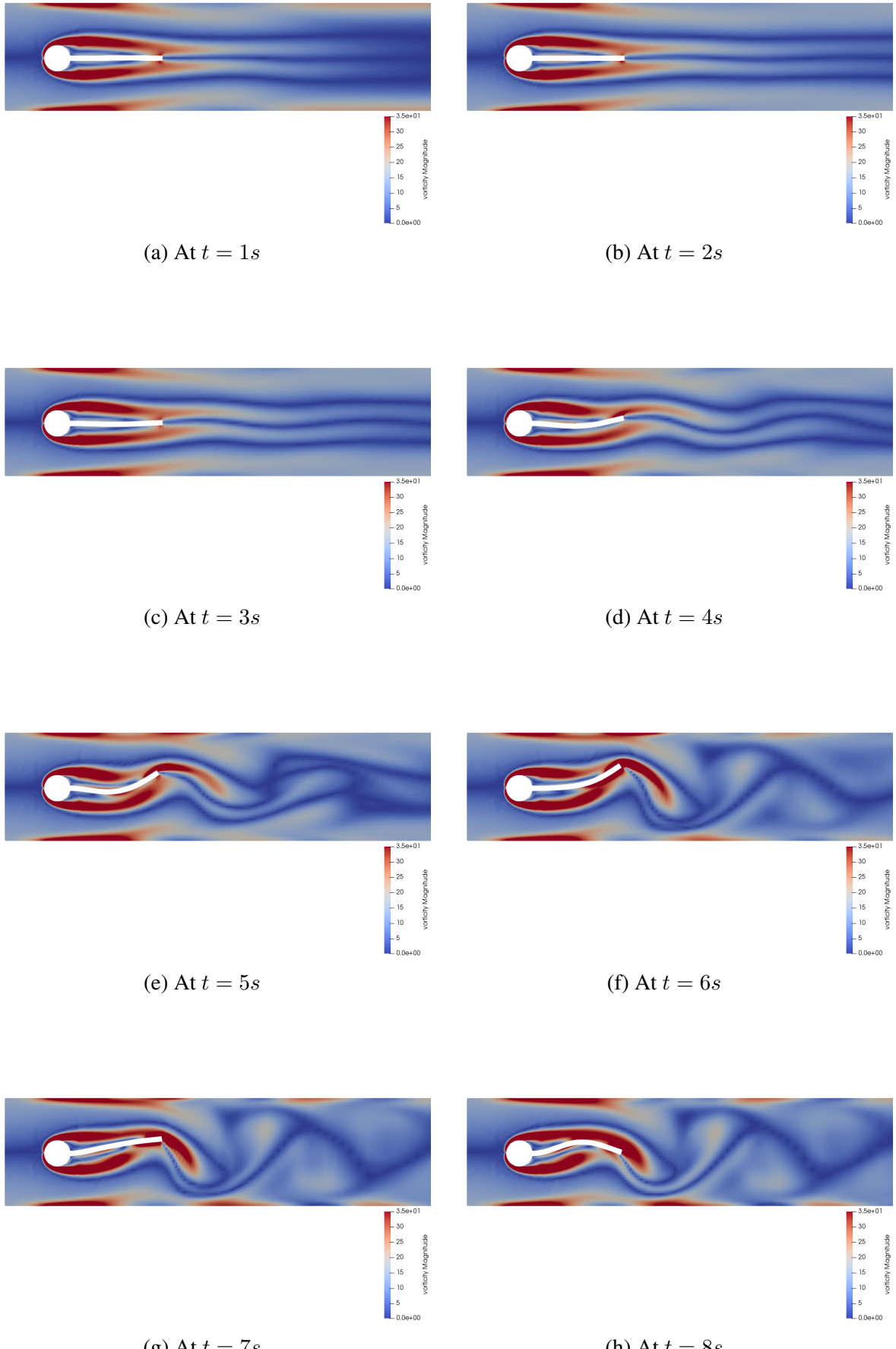
The displacement of the midpoint of the free end of the flap in both horizontal and vertical directions is quantitatively validated with the benchmark in table 2.6. The results are provided for $\rho^s = 10^3 \text{kgm}^{-3}$, $\nu^s=0.4$, $\rho^f = 10^3 \text{kgm}^{-3}$, $\nu^f = 10^{-3} \text{m}^2 \text{s}^{-1}$, and $U=0.2 \text{ms}^{-1}$

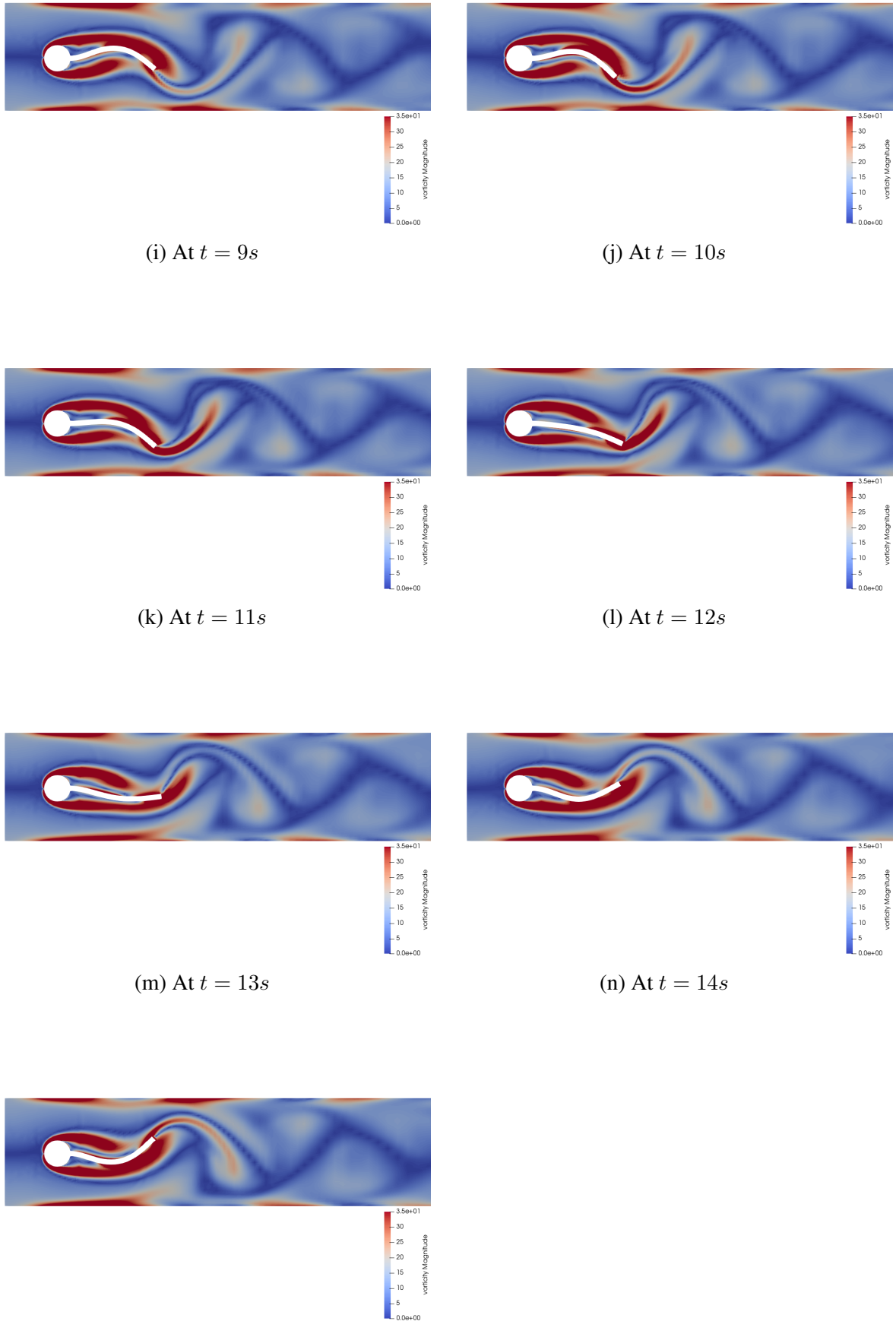
Table 2.6: Quantitative validation of FSI1 with benchmark

Work	Vertical displacement of tip
Present work	0.80602 mm
Turek & Hron (2006) [60]	0.8209 mm

FSI2

In this particular case, flow is described by $Re = 100$. The alternate shedding of vortices, known as von-Karman vortex shedding is formed in the wake region of the cylinder which is a characteristic of unsteady flow over a stationary circular cylinder for Re greater than 47. This alternating vortex shedding results in an oscillating lift force which acts along the cantilever beam. As a result, the flap exhibits oscillations. As it can be seen from the figure 2.22, the deflection of the beam is large. The vortices formed in the wake region can also be seen in the figure 2.22.





The displacement of the midpoint of the free end of the flap in both horizontal and vertical directions is quantitatively validated with the benchmark in table 2.7. The results are provided for $\rho^s = 10^4 \text{kgm}^{-3}$, $\nu^s = 0.4$, $\rho^f = 10^3 \text{kgm}^{-3}$, $\nu^f = 10^{-3} \text{m}^2 \text{s}^{-1}$, and $U = 1 \text{ms}^{-1}$

Table 2.7: Quantitative validation of FSI2 with benchmark

Work	Vertical displacement of the tip
Present work	0.091155
Turek & Hron (2006) [60]	0.08183

FSI3

In this particular case, flow is described by $Re = 200$. Similar to FSI2, there is vortex shedding, resulting in oscillating lift forces which act along the cantilever beam. However, as it can be seen from the figure 2.23, the deflection of the beam is not as large as the one in FSI2. The vortices formed in the wake region can be seen in figure 2.23

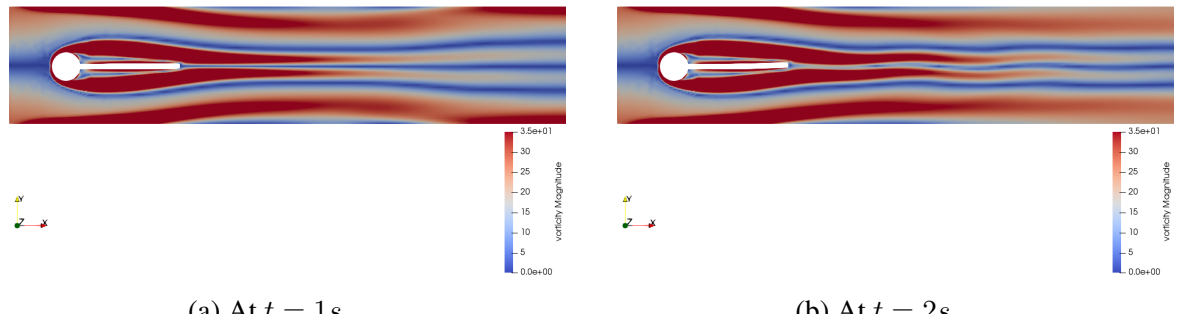
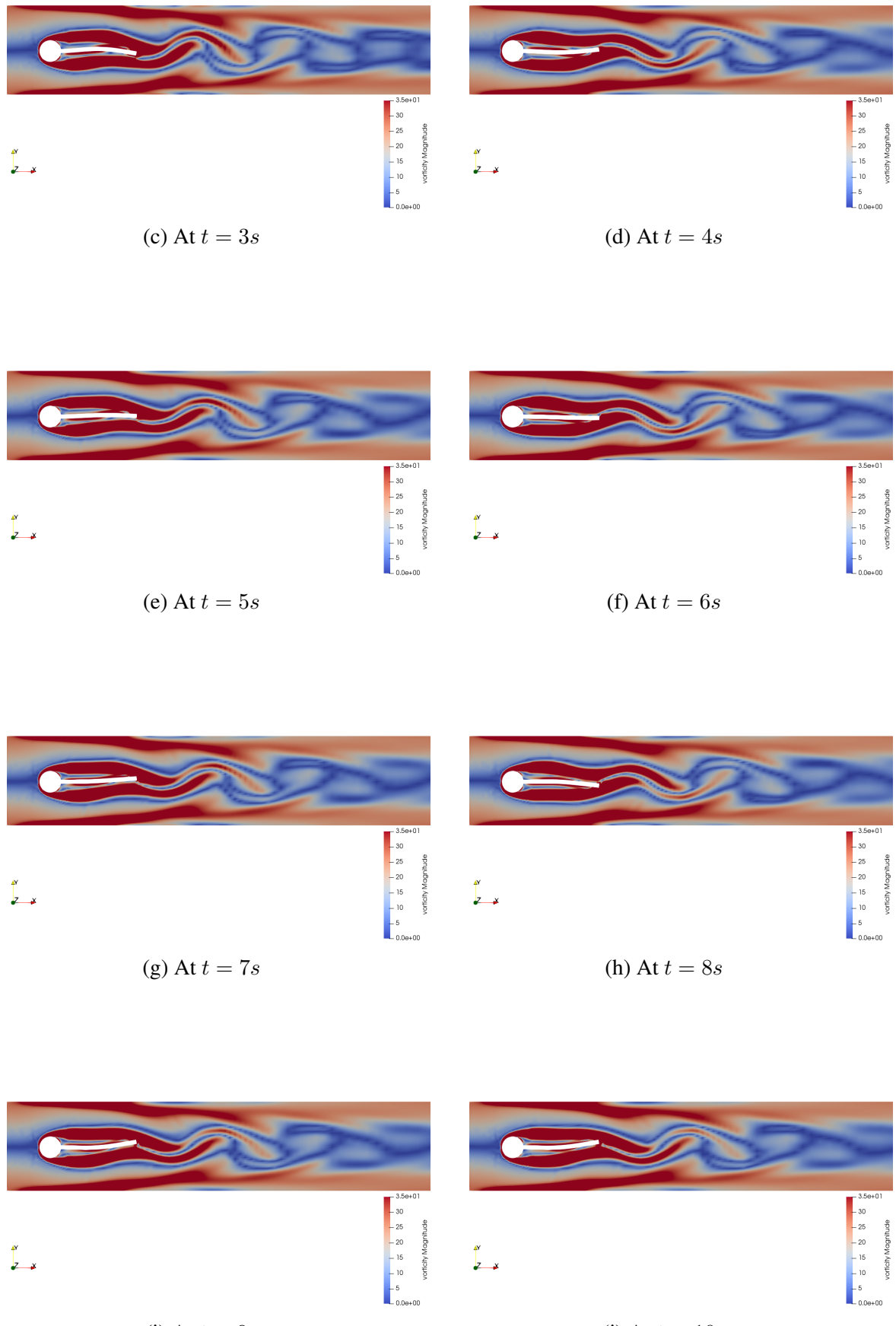


Figure 2.23: Vorticity plots for ESI3 at various instances



The displacement of the midpoint of the free end of the flap in both horizontal and vertical directions is quantitatively validated with the benchmark in table 2.8. The results are provided for $\rho^s = 10^3 \text{kgm}^{-3}$, $\nu^s=0.4$, $\rho^f = 10^3 \text{kgm}^{-3}$, $\nu^f = 10^{-3} \text{m}^2 \text{s}^{-1}$, and $U=2 \text{ms}^{-1}$

Table 2.8: Quantitative validation of FSI3 with benchmark

Work	Vertical displacement
present work	0.030568
Turek & Hron (2006) [60]	0.03568

The case involving steady flow named FSI1 was simple to validate. The cases involving unsteady flow namely FSI2 and FSI3 was highly numerically unstable. Chronologically, this FSI case was first used for validation. Hence, like in the previous divergent simulation, we couldn't pinpoint the reason for divergence on the choice of finite volume schemes. Since this divergence issue was not prevalent in simulating Flow over a Circular Cylinder as described in section 2.5.1, which is similar to the present FSI test case, it was assumed that the divergence was occurring due to the input choices made with the coupling library. Upon approaching the developers of preCICE coupling library, it was made clear that they have been facing the similar difficulty with this particular test case. Upon simulating with every possible configuration, it was clear that the choice of discretization schemes used to model the fluid flow have a significant effect on the numerical stability of the simulation.

In particular, a wrong choice of divergence scheme led to the divergence in this particular case. Divergence scheme is the numerical scheme used to discretize the advection terms. As enquiring the reason behind the effect of the choice of divergence schemes on the numerical simulation doesn't come under the scope of this thesis, the results produced in the divergent simulations for this particular case are provided in fig 2.24. Of all the divergent schemes, the one presented in fig 2.24d gives us an accurate solution. Hence, all the upcoming FSI simulations will utilize this divergence scheme.

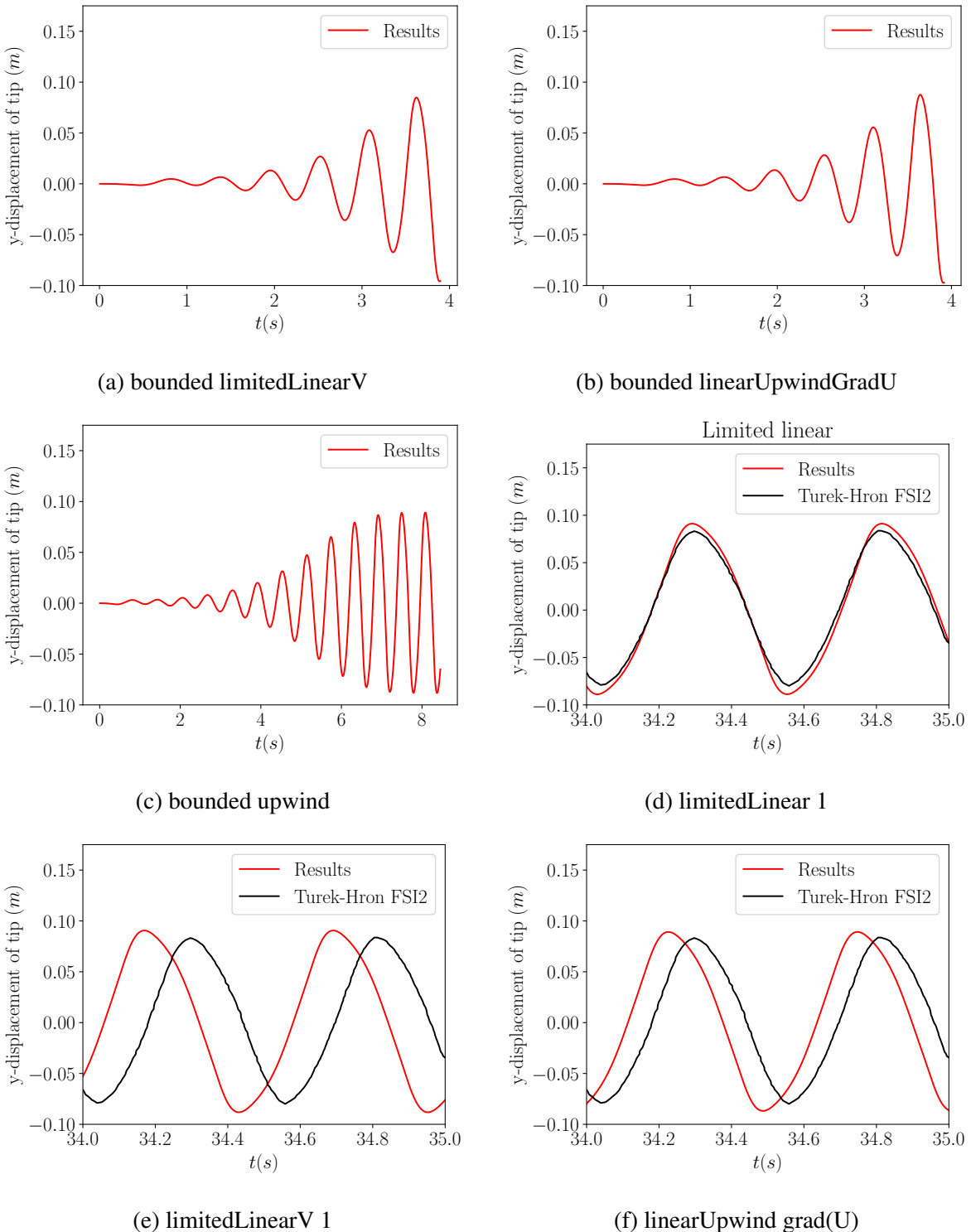


Figure 2.24: Effect of surface normal gradient scheme on numerical stability

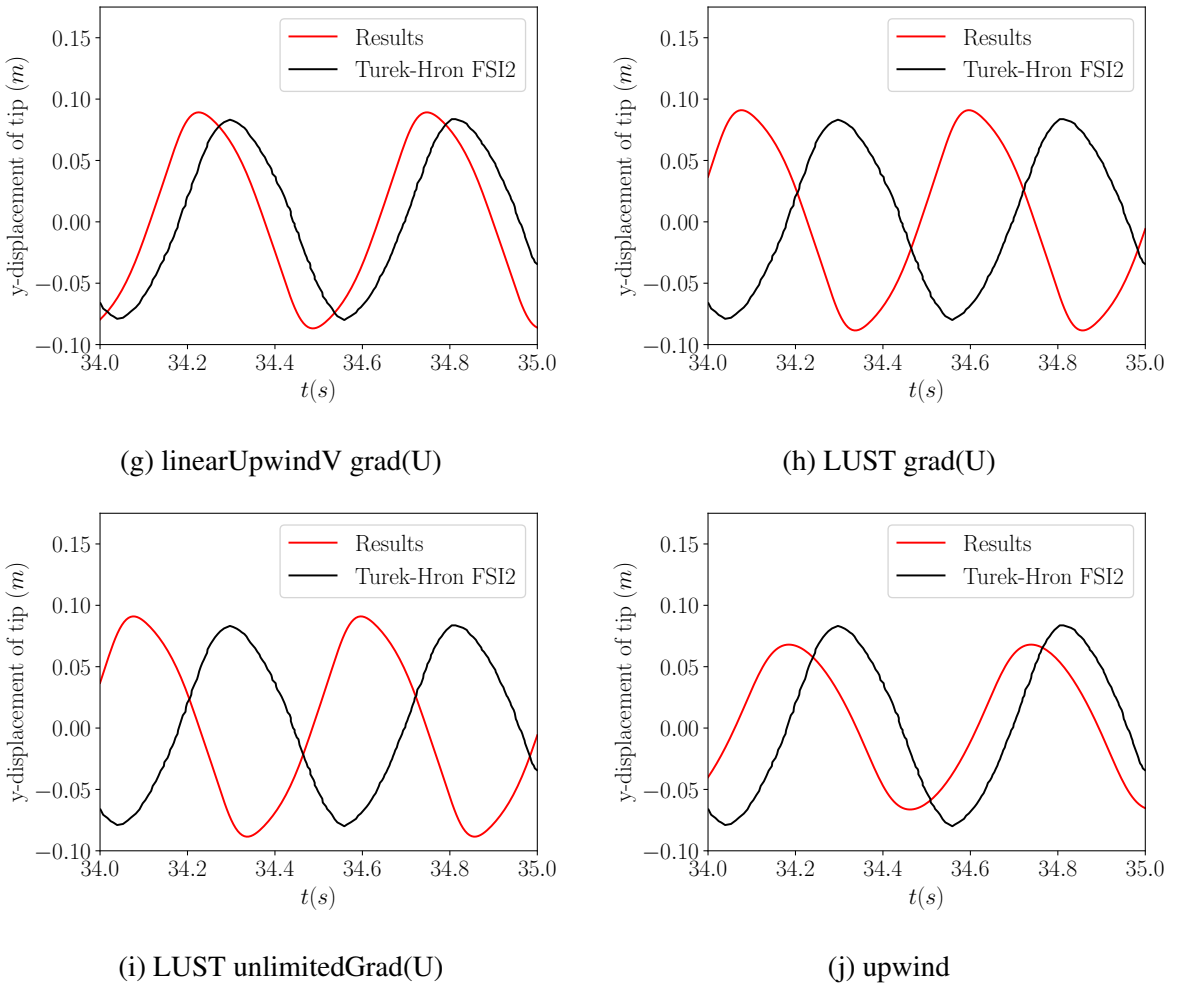


Figure 2.24: Effect of surface sormal gradient scheme on numerical stability (cont)

Chapter 3: Simulations of flapping Wing

3.1 Translating rigid wing

Translational acceleration is an important phase in insect flight. Studying the effect of this acceleration phase gives us an insight to the effect of delayed stall on insect flight. The motivation of this case is to study the stable leading edge vortices and to evaluate for how many stride lengths the effect of fast acceleration persists.

A flatplate at an angle of attack 45^0 is accelerated from rest until it reaches a characteristic velocity and then it translates with that constant velocity until it covers a distance of 7 chord length. The mesh was produced using blockMesh.

The size of the computational domain is $(-8c \leq x \leq 25c, -8c \leq y \leq 8c)$. The center of the top face of the flat-plate is taken as the origin. c is the chord length of the flat-plate which is taken as the characteristic length scale for the simulation. The domain is as shown in figure 3.1.

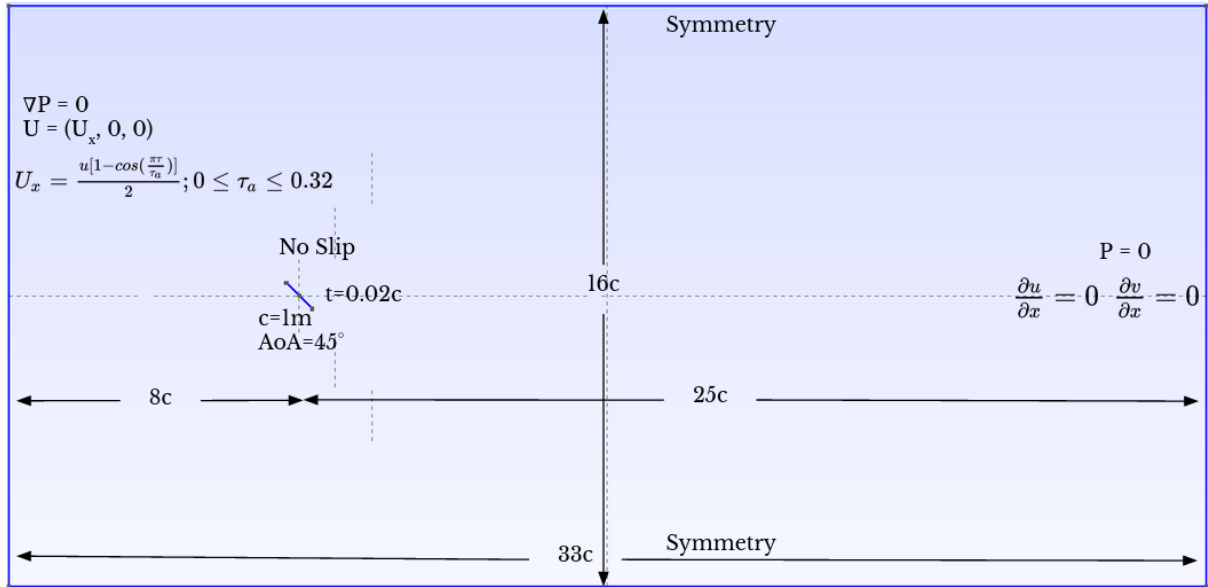


Figure 3.1: Domain used for accelerated flat-plate

The flat-plate is accelerated from rest for a non-dimensional time $\tau_a = 0.32$, to reach a constant non-dimensional velocity $u = 1$. This is done by giving boundary conditions at the inlet, as

$$U_x = u[1 - \cos(\pi \frac{\tau}{\tau_a})]/2 \quad \text{for } 0 \leq \tau \leq 0.32$$

$$U_x = 1 \quad \text{for } \tau > 0.32$$

$U_y = 0$, $U_z = 0$ and a Neumann condition for pressure is applied by keeping $\nabla P = 0$. At the outlet, a Neumann condition for velocity is applied by keeping $\frac{\partial u}{\partial x} = 0$, $\frac{\partial v}{\partial x} = 0$ and a Dirichlet

condition for pressure is applied by keeping $P = 0$. A symmetry condition is maintained at the top and bottom. A no-slip condition is maintained on the periphery of the flatplate. The inlet velocity u is taken as the characteristic velocity scale. The simulation is conducted with $Re = 212$

The force coefficients are calculated. As expected, we see a spike in the forces during the acceleration phase. This acceleration has an effect on the flight characteristics until 7 chord lengths are traversed after which steady state force values are obtained. The force coefficients are over predicted during the acceleration phase. Apart from that, the force coefficients agree with the ones presented in Miller and Peskin (2004) [61] or Dickinson and Gotz (1993) [14]. The comparison of force coefficients obtained with those from the literature are plotted against the chord lengths travelled is not shown as the forces are over predicted during the acceleration phase. The reason for this over-prediction is being investigated.

3.2 Translating flexible wing

Flexibility study was conducted on the earlier case Translating rigid wing to study how flexibility might effect the leading edge vortex produced during the acceleration phase. To do this 50% of the earlier flat-plate is made rigid and the rest 50% is made flexible with a flexural rigidity in the range of flexural rigidities of most insects. The method used to conduct the FSI study is similar to the validation cases from chapter 2.

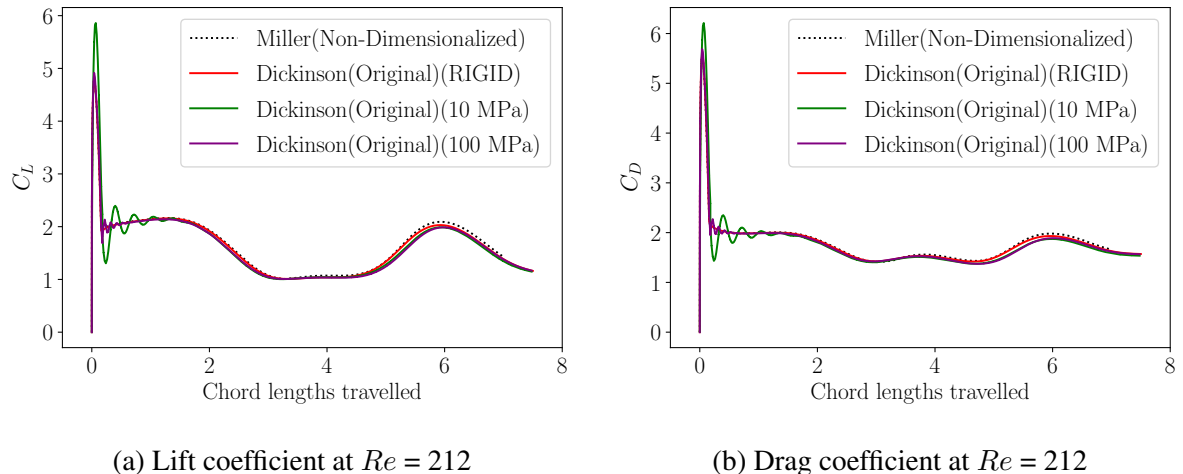
The fluid domain and boundary conditions are maintained exactly the same as the earlier case. The flexible part of the insect wing is modelled as a cantilever beam which is discretized into 80 elements (80 along length, 1 along height and 1 along thickness). The elements used here are reduced-integration quadratic beam elements (he20r). One end of the beam attached to the rigid part is fixed by arresting the corresponding nodes in space, constraining all their degrees of freedom. At the free end of the beam, the nodes are not allowed to move in the z-direction. Rotation along all the axes is restrained for nodes all throughout the beam. The length of the beam is $0.5c$, height $0.02c$. The elastic modulus of the isotropic beam is 10 MPa and its Poisson's ratio is 0.

The force coefficients on the flexible insect wing are calculated. They are compared to the force coefficients on rigid wings. The results are presented in fig 3.2. There are two hurdles to firmly establish the effect of flexibility on delayed stall.

1. The force coefficients for the rigid wing are over predicted during the acceleration phase.
 2. The flexible wing oscillates even after the immediate effect of acceleration is vanished.
- These can be seen as oscillations of force coefficients in fig 3.2

Rigid wing translating wing according to Miller and Peskin (2004) [61] is labeled as Miller(Non-Dimensionalized) and the rigid translating wing according to Dickinson and Gotz (1993) [14] is labeled as Dickinson(Original)(Rigid). The translating flexible wings following Dickinson and Gotz (1993) [14] but with a 50% flexible wing of Elastic Modulus 10 MPa is labeled as

Dickinson(Original)(10MPa) and 50% flexible wing of Elastic Modulus 100 MPa is labeled as Dickinson(Original)(100MPa)



(a) Lift coefficient at $Re = 212$

(b) Drag coefficient at $Re = 212$

Figure 3.2: Comparison of force coefficients, rigid wing vs flexible wing

3.3 Fruitfly Kinematics using overset mesh

Characteristic studies conducted on insects have usually been conducted on the fruitfly. Fruitfly kinematics offer a comprehensive understanding of the phenomena involved in insect flight, from rotational effects to wing-wake interactions, and thus validating results for one full flapping stroke is of great importance. Unlike previous studies, OpenFOAM v1912 was used for this simulation as OpenFOAM 7 isn't compatible with overset meshes.

In particular, a flatplate of length L and width $0.02L$ was used as an approximation to the 2D cross-section of the fruitfly's wing. Computational domain used was from $(-10L \leq x \leq 5L; -7L \leq y \leq 7L)$. For ease in simulation an overset mesh was used containing the flatplate as shown in figure 3.4. The smaller mesh has a domain of $(-0.7L \leq x \leq 1.3L; -1.01L \leq y \leq 1.01L)$, with the flatplate present in the region $(-0.2L \leq x \leq 0.8L; -0.01L \leq y \leq 0.01L)$.

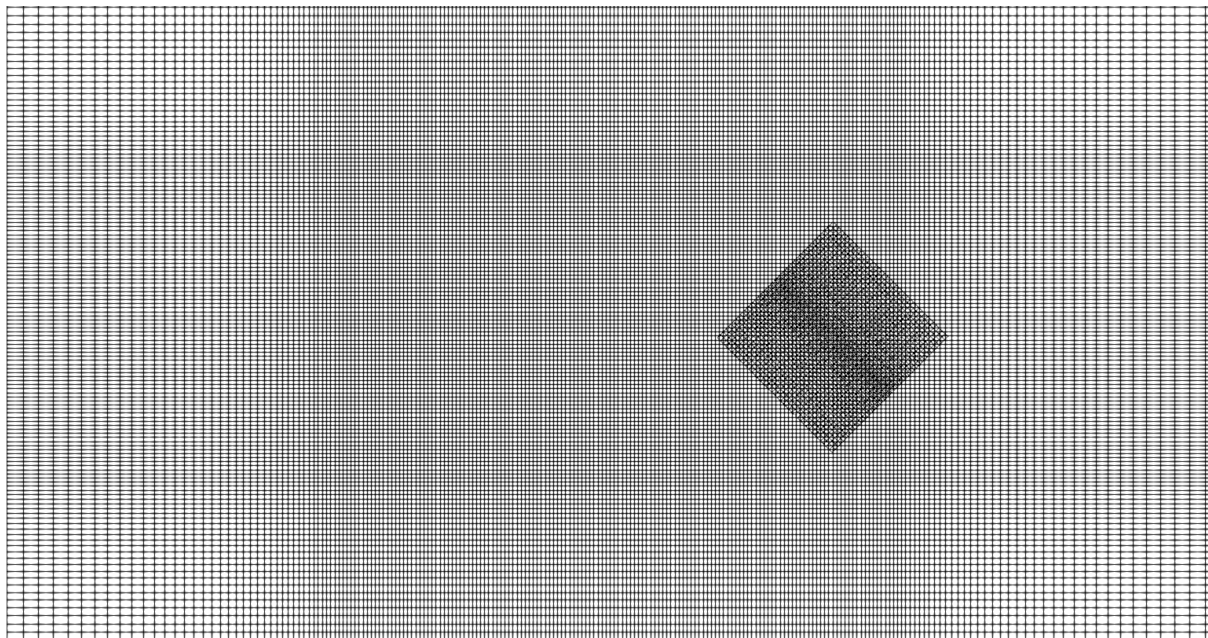


Figure 3.3: Depiction of background mesh

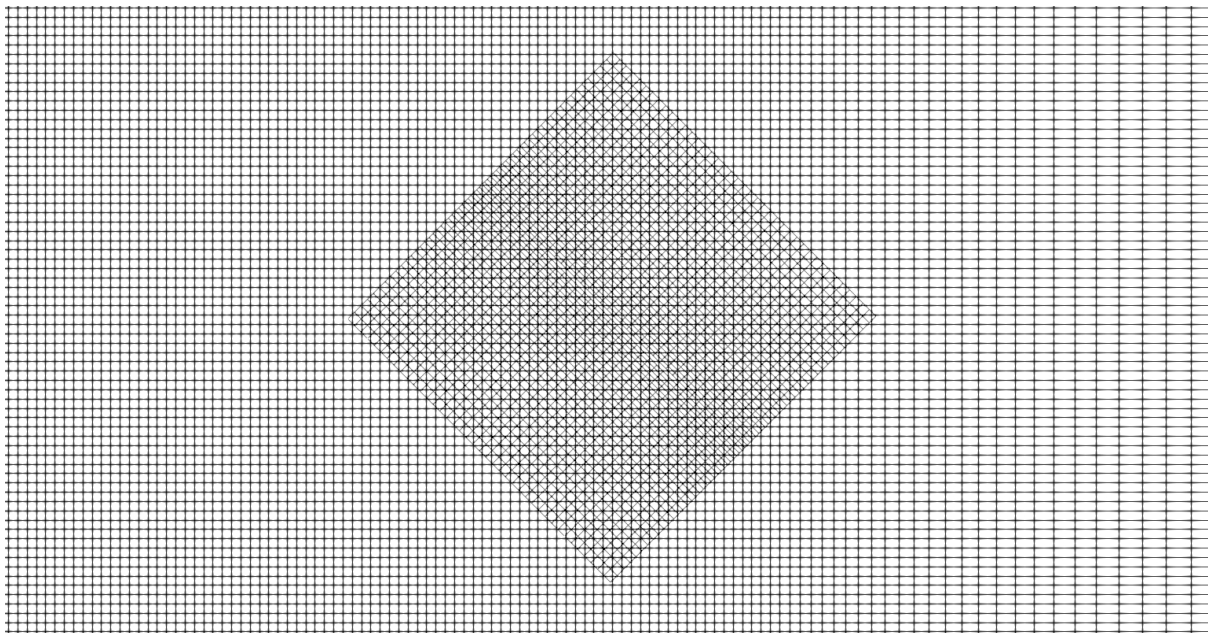


Figure 3.4: Closeup of subsidiary mesh

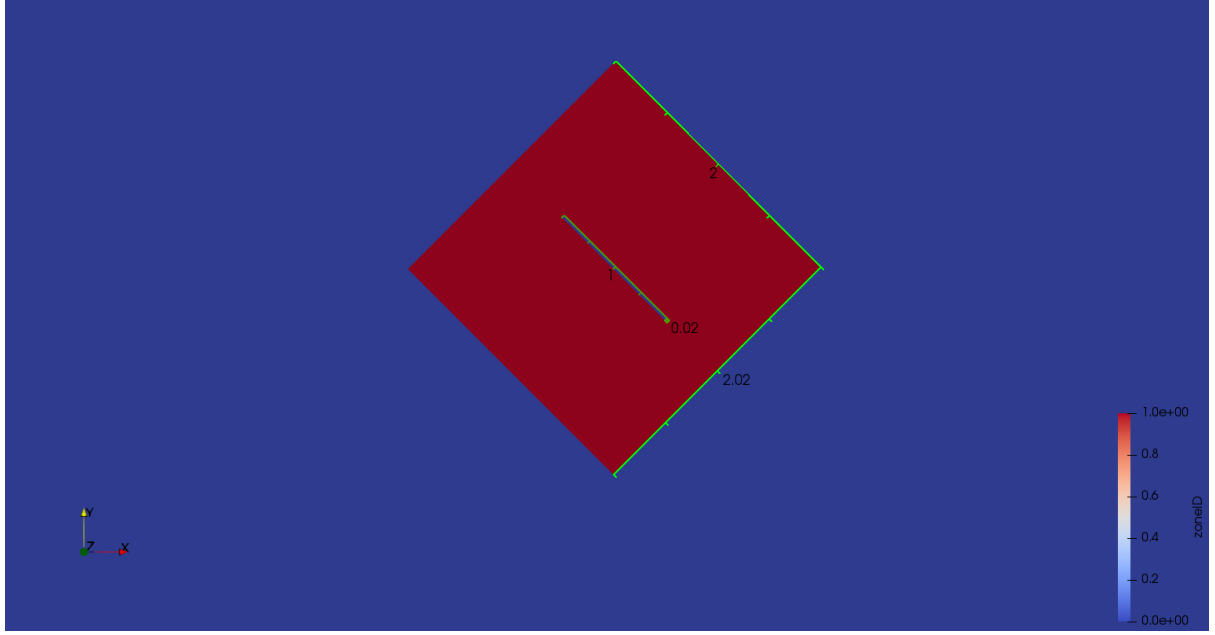


Figure 3.5: Cells from the 2 overlapping meshes

For this, at the left and right edges of the boundary, the $\frac{\partial u}{\partial x} = \frac{\partial v}{\partial x} = 0$, and $\frac{\partial u}{\partial y} = v = 0$ at the top and bottom. On the moving flatplate, $u_{fp} = u_f$ and $v_{fp} = v_f$, where u_{fp} and v_{fp} indicate the x and y velocities of the moving plate, while u_f and v_f denote the x and y velocities of the fluid.

The motion of the fruitfly consists of an upstroke and a downstroke phase. In both these phases, there is an accelerating phase and a decelerating phase, as well as a constant velocity phase in between. In addition, there is rotation about a point $0.2L$ from the leading edge of the wing around the end of the downstroke phase. Only first flapping cycle is considered here, in order to validate Miller and Peskin(2004) [61]. During the acceleration phase at the beginning of the half-stroke, the velocity is given by

$$v(\tau) = \frac{1}{2}V[1 + \cos(\pi + \frac{\pi\tau}{\Delta\tau_{trans}})]$$

$$\tau = \frac{tV}{c}$$

where v is the translational velocity at dimensionless time τ , t is the actual time, V is the stroke velocity at the end of acceleration, $\Delta\tau_{trans}$ is the dimensionless duration of both acceleration and deceleration and c is the chord length of the wing.

After this phase, the wing travels with constant translational velocity, V . Deceleration of the wing at the end of the half stroke is given by

$$v(\tau) = \frac{1}{2}V[1 + \cos(\pi \frac{\tau - \tau_d}{\Delta\tau_{trans}})]$$

The wing rotates about $0.2L$ from the leading edge. The angular velocity during the rotational phase is given by

$$\theta(\tau) = \frac{1}{2}\theta_{rot}[1 - \cos(2\pi\frac{\tau - \tau_{rot}}{\Delta\tau_{rot}})]$$

$$\theta_{rot} = \frac{2\Delta\theta V}{\Delta\tau_{rot}c}$$

where θ_{rot} is a constant determined by the distance of rotation and duration of the rotational phase, $\Delta\tau_{rot}$ is the duration of rotational phase, τ_{rot} is the time at which the rotation begins, $\Delta\theta$ is the angular distance over which the rotation occurs.

In our simulations, the parameters are set at the following values: $V = 1$, $L = 1$, kinematic viscosity (ν) adjusted in such a way that $Re = 128$, $\tau_{final} = 10.8$, $\Delta\tau_{trans} = 0.65$, angle of attack during both downstroke and upstroke are 45^0 , $\Delta\theta = 90^0$, $\tau_{rot} = 3$ and $\Delta\tau_{rot} = 3.48$

The subsidiary mesh is rotated and moved according to these equations. The vorticity plots at various points are shown in figure 3.6. You can clearly see the involvement of the leading edge vortex and its development and shedding over the course of a full flapping cycle clearly in these images.

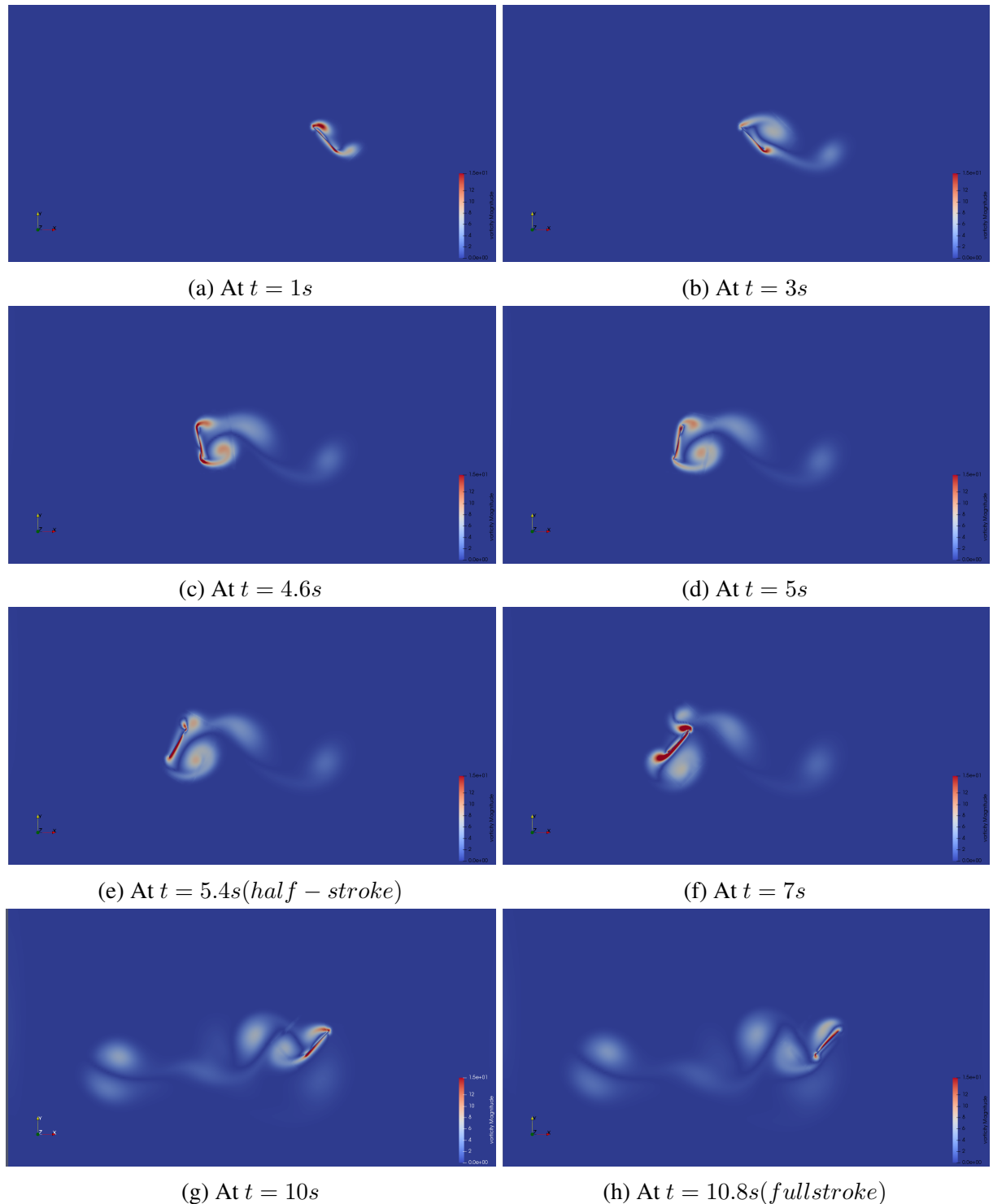


Figure 3.6: Vorticity plots for one full stroke involving fruitfly kinematics

The force coefficients all through the stroke are compared with results from Miller-Peskin(2004) [61], and are plotted as shown in figure 3.7.

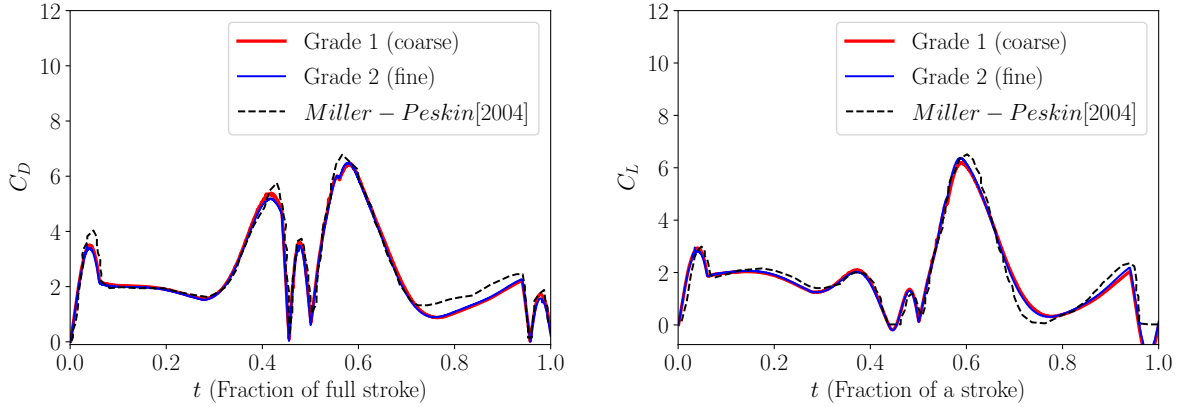


Figure 3.7: Comparision of force coefficients over one full-stroke

3.4 Fruit fly kinematics using Arbitrary Mesh Interface

Movement in conventional meshes is limited, and cases like fruitfly kinematics are impossible to implement if you are actually moving the mesh due to the breaking of the mesh. Thus, initially to overcome this we used Arbitrary Mesh Interfacing(AMI) to allow for rotation and applied the boundary conditions of the fruitfly kinematics case as inputs in velocity. AMI allows us to rotate certain parts of the mesh as there are no actual grids between certain set of points, but they do communicate virtually. The difference between AMI and normal meshes is that this communication is always between fixed set of nodes, and these neighbouring nodes are always the same in the case for a normal mesh. However, AMI means that the neighbouring nodes are dynamically varying and are calculated during solving. This means a computational cost is paid, but the flexibility like in overset meshes is desired. The mesh used is shown in the figure 3.8

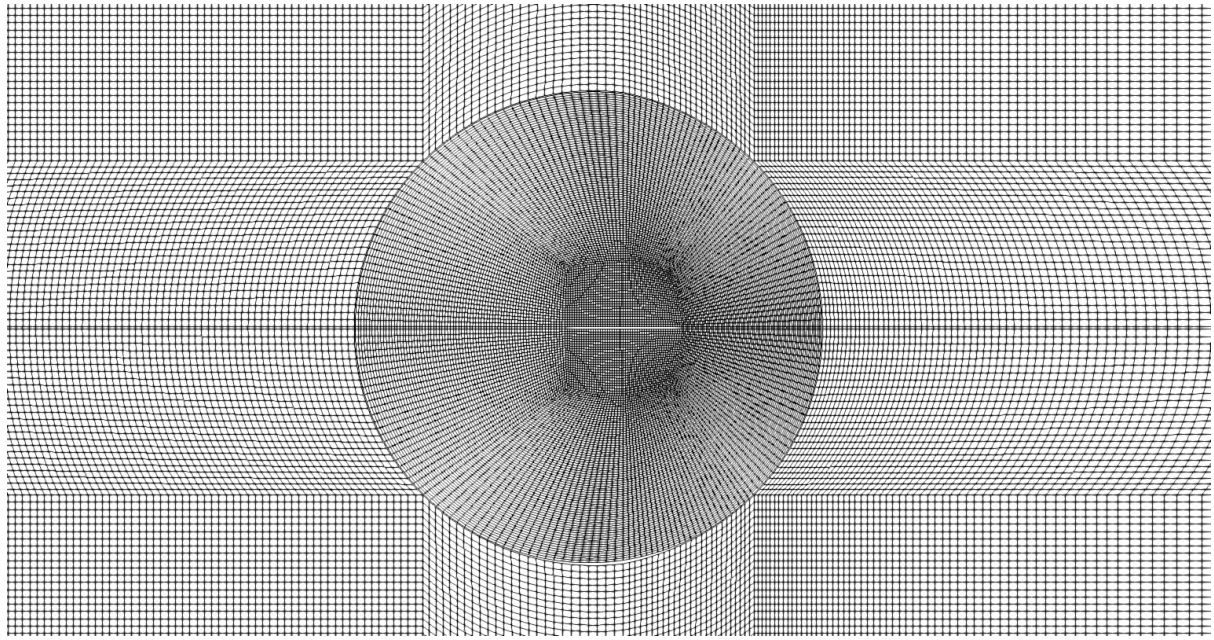


Figure 3.8: Mesh for fruitfly case with AMI

For this, at the right edge of the boundary, the $\frac{\partial u}{\partial x} = \frac{\partial v}{\partial x} = 0$, and $\frac{\partial u}{\partial y} = v = 0$ at the top and bottom. On the moving flatplate, $u_{fp} = u_f$ and $v_{fp} = v_f$, where u_{fp} and v_{fp} indicate the x and y velocities of the moving plate, while u_f and v_f denote the x and y velocities of the fluid. The left edge has input velocity given according to equations in fruitfly kinematics. Vorticity plots from these are given in figure 3.9

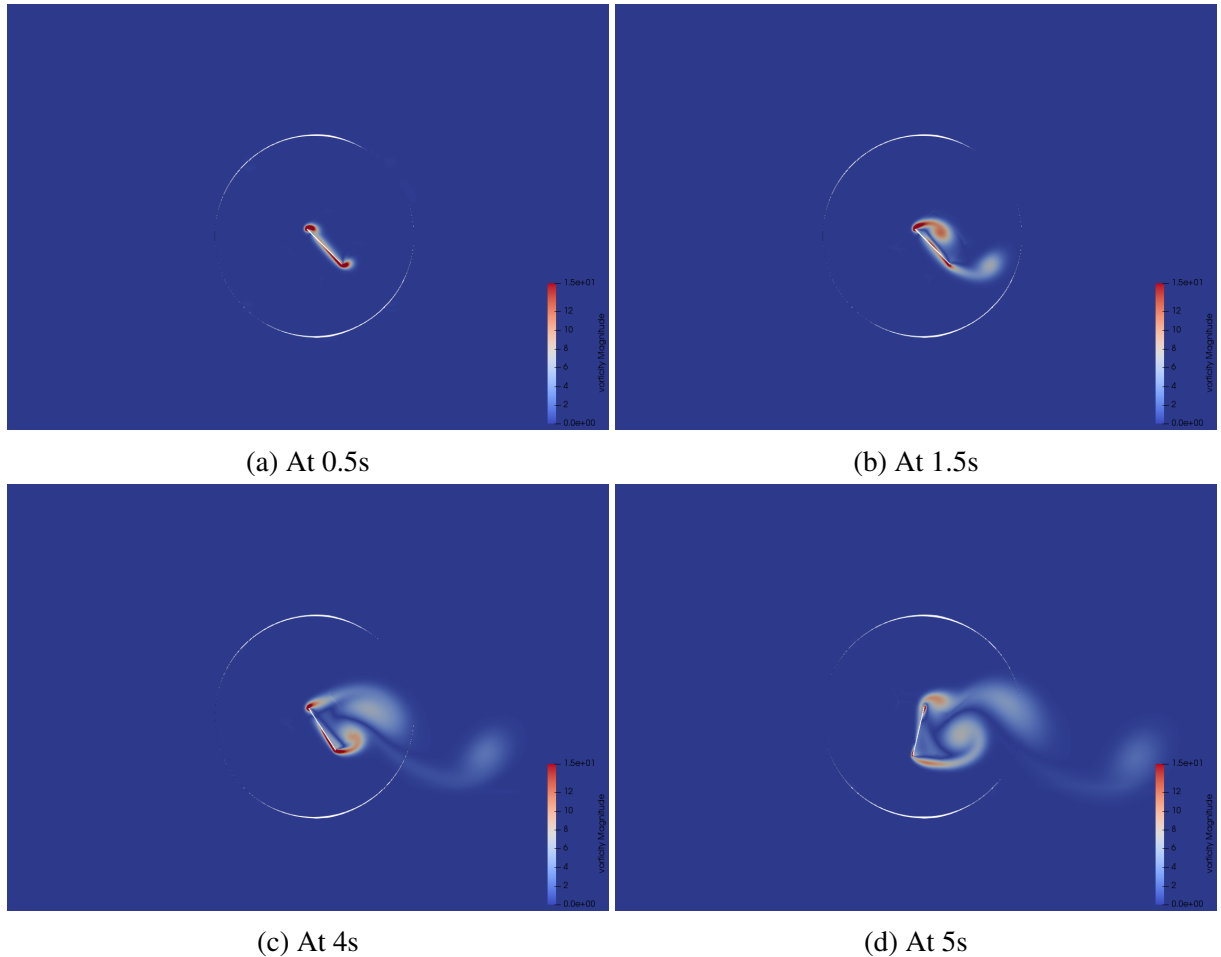


Figure 3.9: Vorticity plots at different times

Even though we ran it for 6 full strokes assuming that we would get good results after the first 2-3 flapping cycles, we couldn't get the validation we required. This is why we switched to overset meshes to validate. The C_D and C_L plots using AMI and compared with literature is given in figure 3.10 to figure 3.14

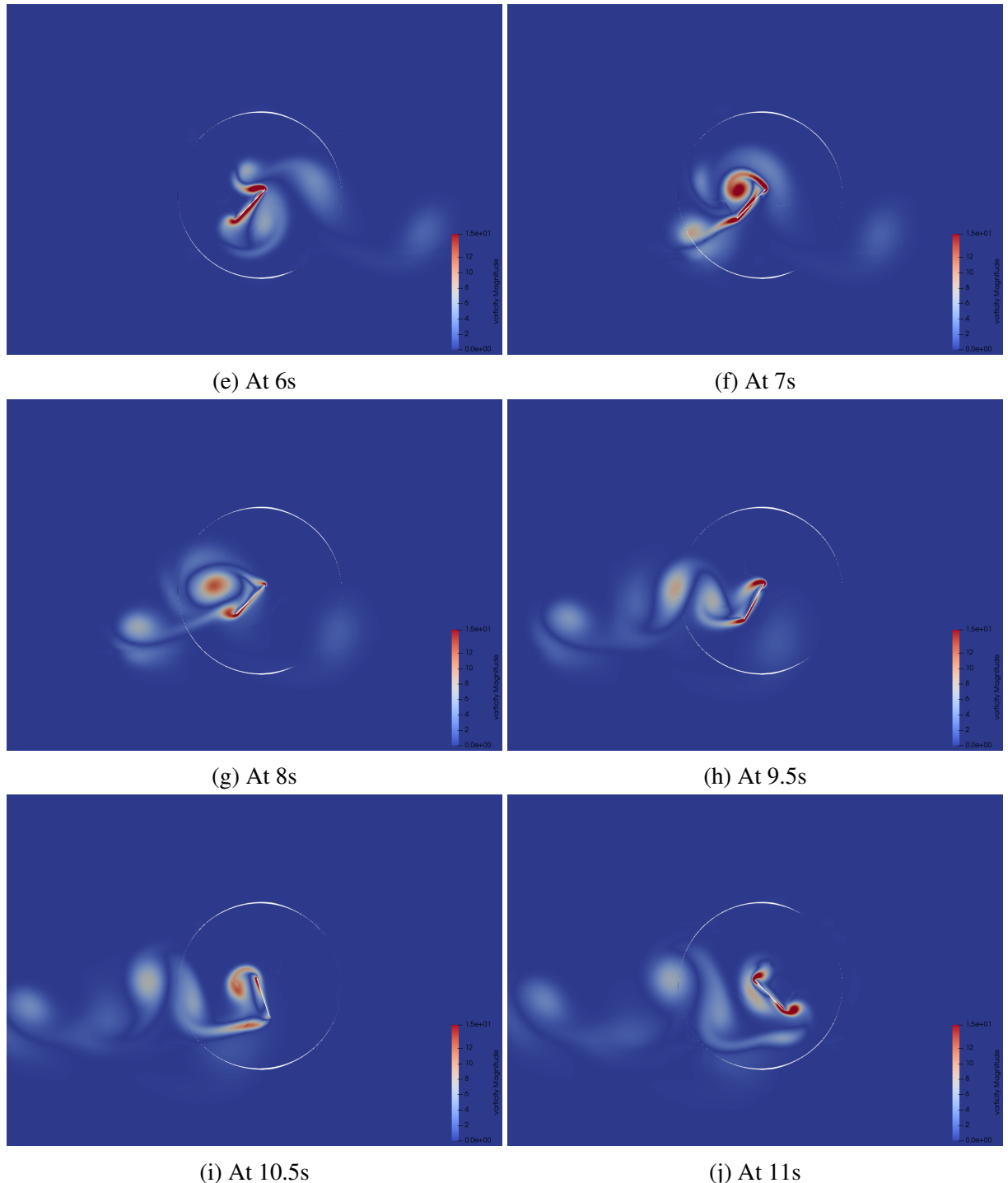


Figure 3.9: Vorticity plots at different times(cont)

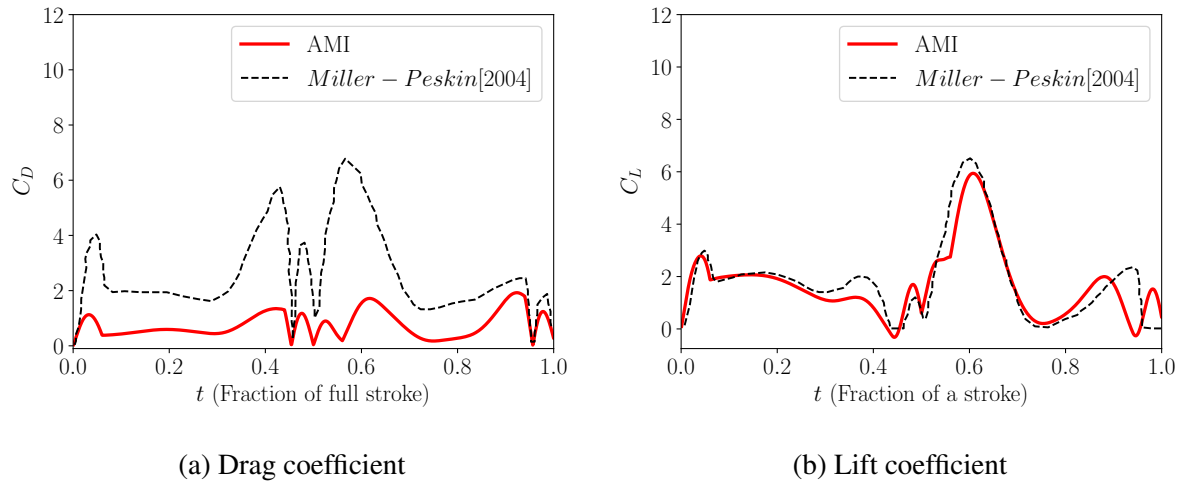


Figure 3.10: Results for the first flap cycle

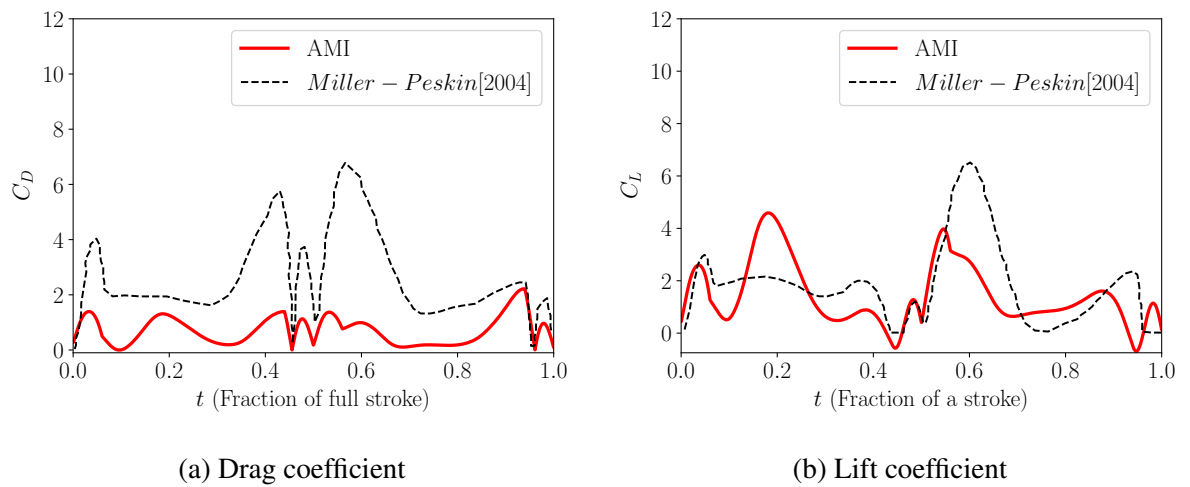


Figure 3.11: Results for the second flap cycle

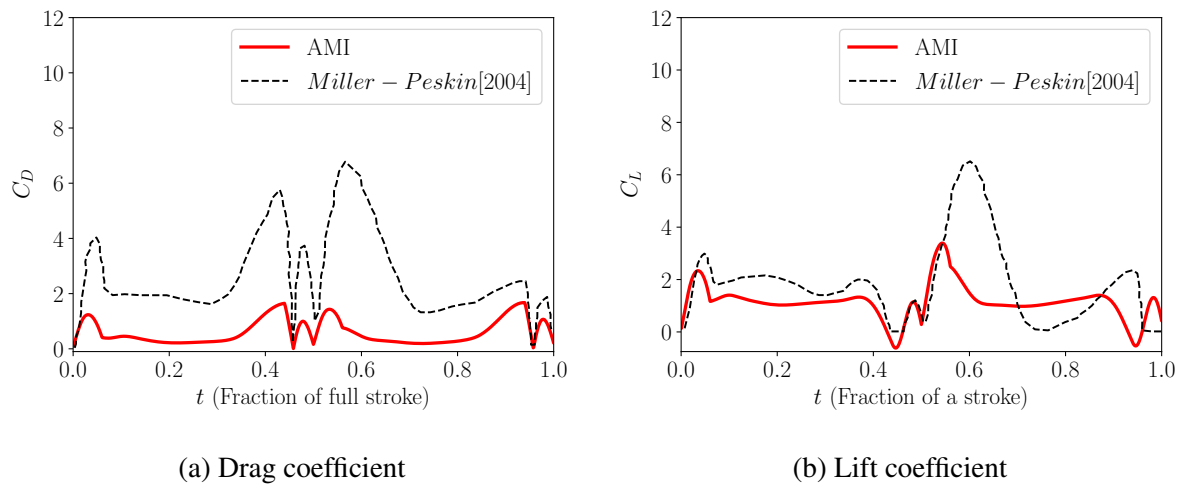


Figure 3.12: Results for the third flap cycle

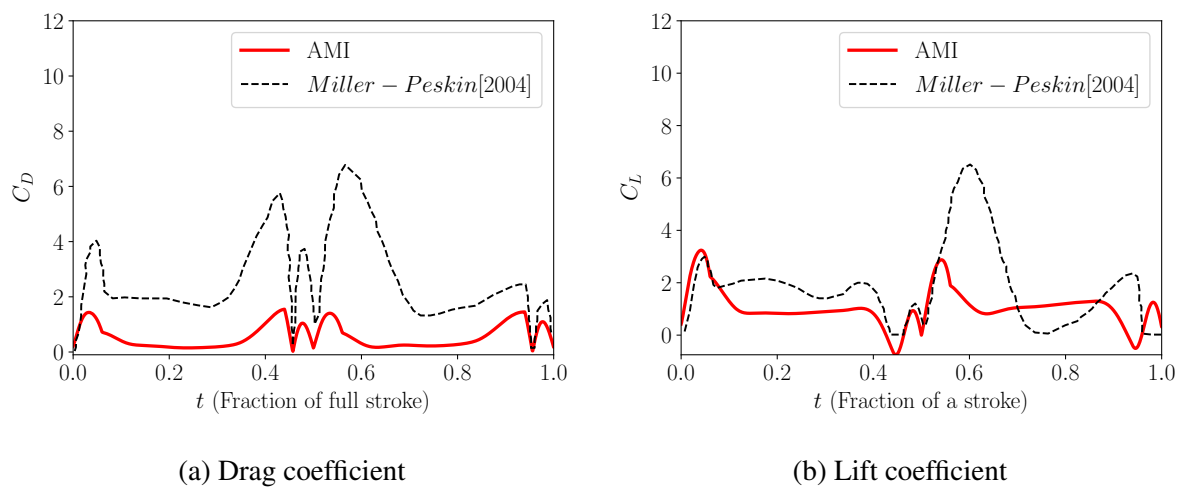


Figure 3.13: Results for the fourth flap cycle

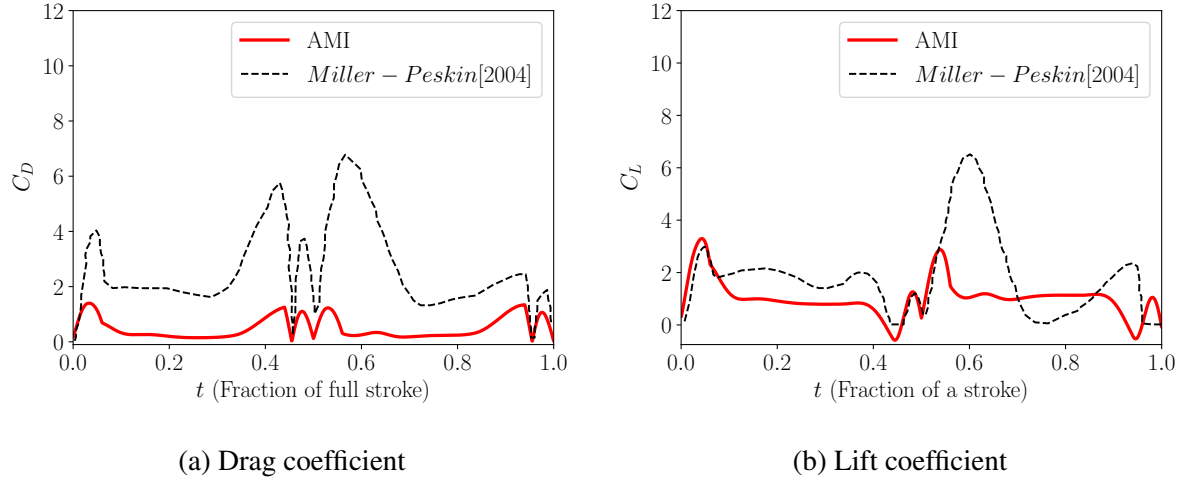


Figure 3.14: Results for the fifth flap cycle

3.5 Dragonfly kinematics using a flatplate

Dragonfly kinematics is another field that is well-studied in the field of insect aerodynamics. This case also differs from the fruitfly kinematics in that the stroke plane is inclined to the horizontal plane and direction of horizontal motion. Here, we try to validate Wang(2000) [62] in non-dimensional form. The mesh used can be seen in figure 3.15 and figure 3.16

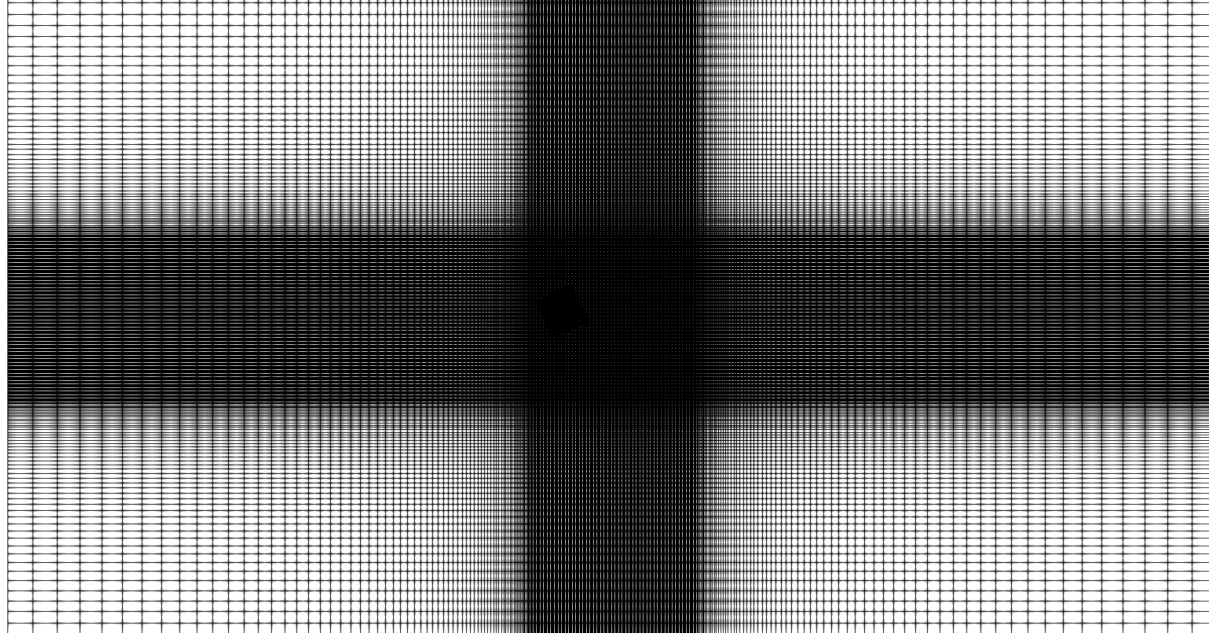


Figure 3.15: Depiction of background mesh

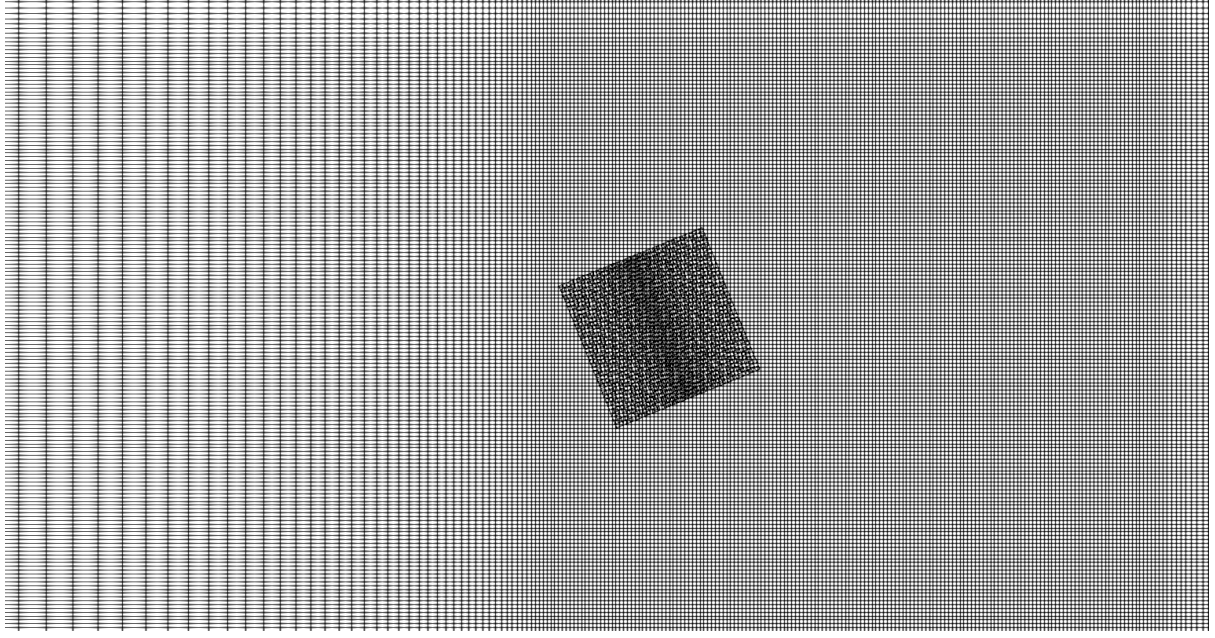


Figure 3.16: Closeup of subsidiary mesh

The computational domain is given by $(-30L \leq x \leq 30L, -30L \leq y \leq 30L)$. For this, at the left and right edges of the boundary, the $\frac{\partial u}{\partial x} = \frac{\partial v}{\partial x} = 0$, and $\frac{\partial u}{\partial y} = v = 0$ at the top and bottom. On the moving flatplate, $u_{fp} = u_f$ and $v_{fp} = v_f$, where u_{fp} and v_{fp} indicate the x and y velocities of the moving plate, while u_f and v_f denote the x and y velocities of the fluid. The wing's motion can be described by

$$[x(t), y(t)] = \frac{A_0}{2} [1 + \cos(2\frac{L}{A_0}t)] (\cos\beta, \sin\beta)$$

and

$$\alpha(t) = \alpha_0 + B \sin[2\frac{L}{A_0}t + \psi]$$

where $[x(t), y(t)]$ is the instantaneous position of the center of the chord, $\alpha(t)$ is the instantaneous angle of attack, β is the stroke plane angle, A_0 and B are amplitudes of translation and rotation respectively, L is the chord length of the wing, α_0 is the mean angle of attack, and ψ is the phase delay between translation and rotation.

Unlike fruitfly kinematics, the wing rotates about the center of the chord, and the instantaneous forces are non-dimensionalized by $0.5\rho v_{rms}^2 L$. Following Wang(2000) [62], the parameters that define the wing motion are as follows: $Re = 157$, $A_0/L = 2.5$, $B = \pi/4$, $\alpha_0 = \pi/4$, $\beta = \pi/3$ and $\psi = 0$.

The vorticity plots at different points in a full stroke are shown in figure 3.17. So far the quantitative validation couldn't be completed.

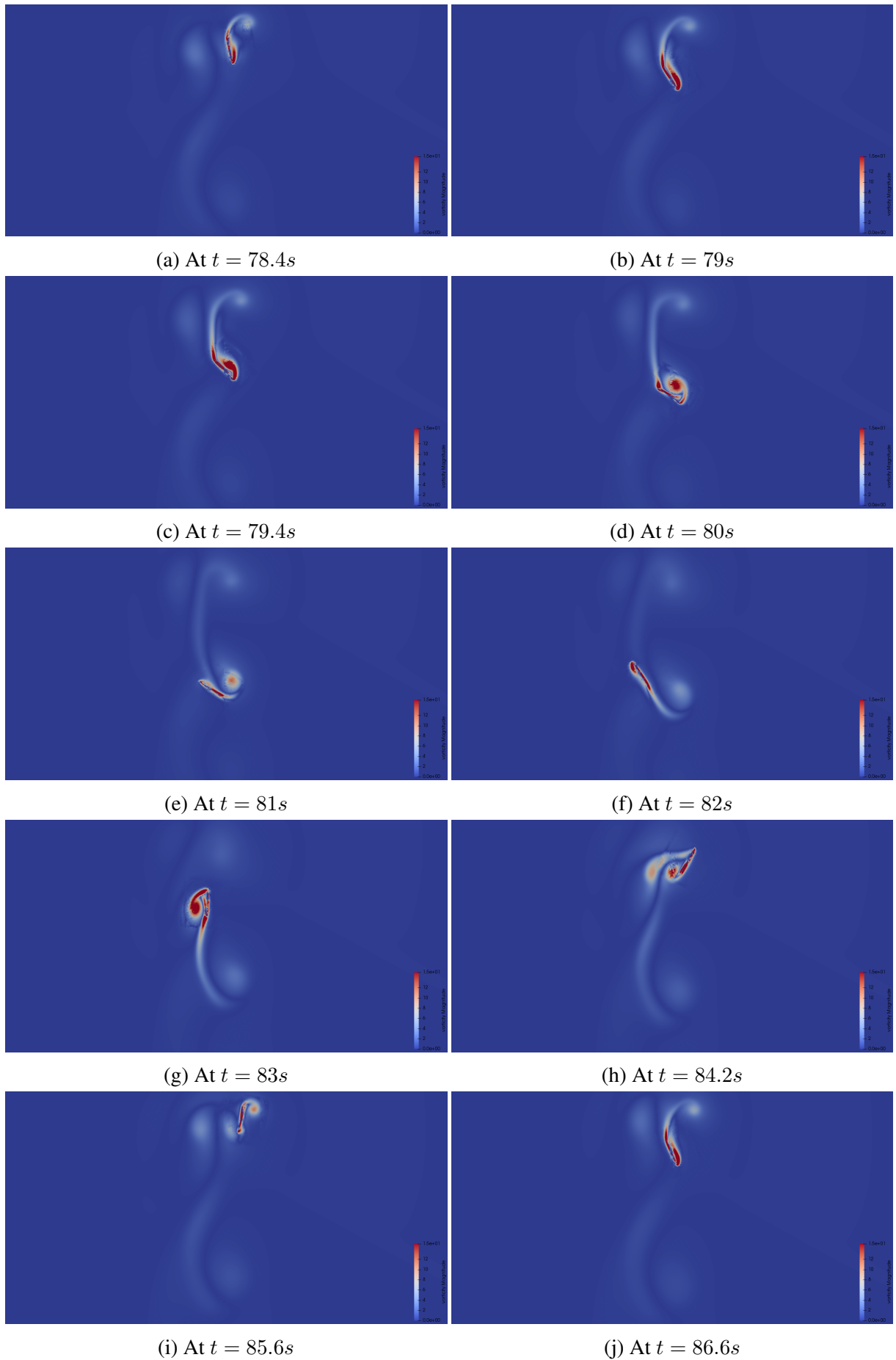


Figure 3.17: Vorticity plots for one full stroke involving dragonfly kinematics

3.6 Dragonfly kinematics using an ellipse

The same case dragonfly case was repeated with an ellipse instead of a flatplate of specified dimensions. In this case, the subsidiary mesh was unstructured and generated using *gmsh*. The results were similar to the case of the flatplate, and even here quantitative validation wasn't possible. The mesh used can be seen in figure 3.18 and figure 3.19.

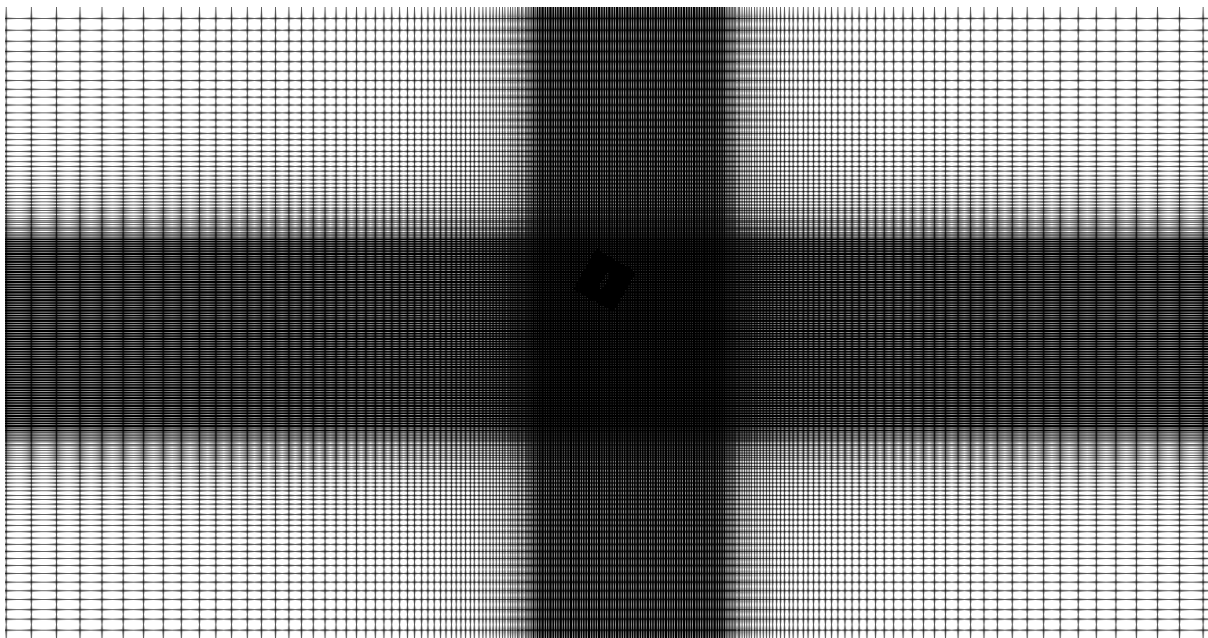


Figure 3.18: Depiction of background mesh

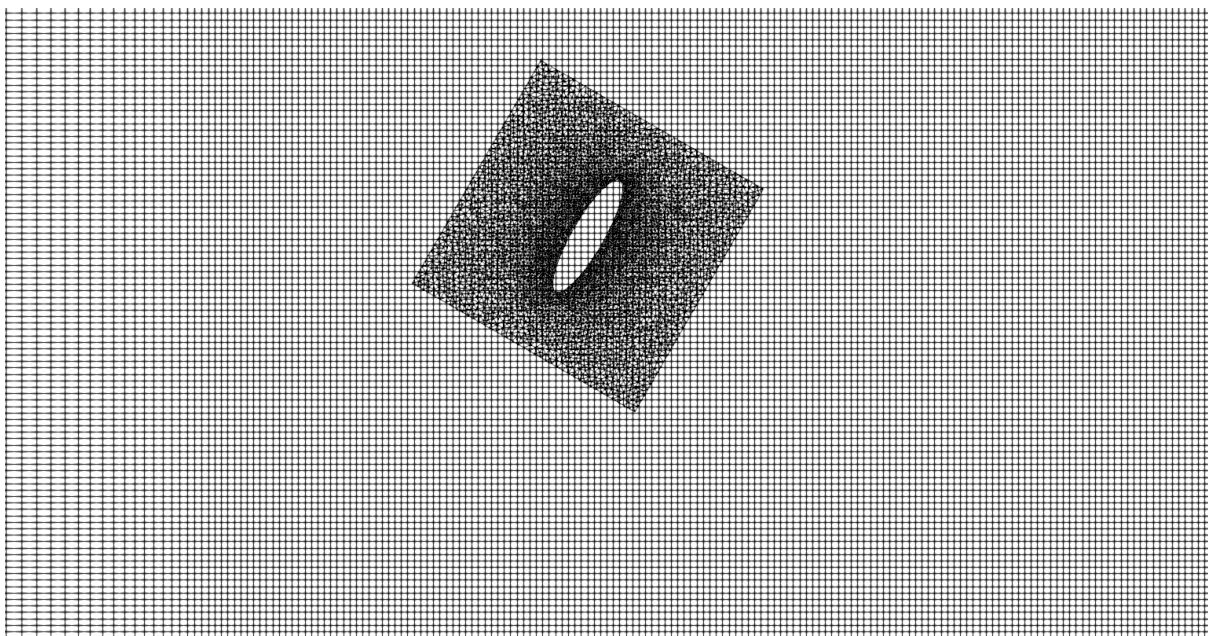


Figure 3.19: Closeup of subsidiary mesh

Chapter 4: Conclusions

4.1 Conclusions

In the present work, various techniques were explored to conduct fluid-structure interaction studies using open-source tools with the primary aim to model insect flight with the core idea that insect wings are flexible. A strongly-coupled partitioned approach was chosen to conduct the study. OpenFOAM, an open-source CFD toolbox was chosen to simulate viscous incompressible flow. The capability of OpenFOAM to carry out the fluid part of the FSI study is established by conducting validation studies. During that process, various fluid dynamics concepts like alternate vortex shedding, von Karman vortex street were studied. CalculiX, an open-source finite-element analysis application was chosen to solve the linear and non-linear structural dynamics equations over a flexible solid body suspended in fluid flow. The accuracy of CalculiX to carry out the structural part of the FSI study involving large deflections is established by conducting validation studies taking geometric non-linearity into consideration. During the process, various finite-element analysis concepts like shear-locking, dynamic stepping were studied. After proving viable both these solvers are coupled using an open-source coupling library preCICE. The capability of this methodology to conduct FSI studies was established with the help of standard FSI test cases. After establishing the capability of this model to conduct FSI study, this was extended to study the effects of flexibility on aerodynamic forces and fields in insect flight.

The effect of delayed stall in inclined stroke motion during the translational phase of an insect was studied. It was postulated the aerodynamic forces produced in a flexible wings would be completely different from those produced by rigid wings. In the present work, the model employed predicted an increase in the lift forces when flexible wing is used compared to a rigid wing as explained in section 3.2. 2-dimensional flapping wing models were generated which could emulate fruit fly aerodynamics as seen in sections 3.4 & 3.4 and dragonfly aerodynamics as seen in sections 3.5 & 3.6. As the conventional meshes used earlier were not successful in accurately predicting the aerodynamic forces during this complicated motion. Techniques involving Arbitrary Mesh Interfaces, Overset mesh were explored to do this and Overset meshes were chosen even though they are computationally expensive. The methodology has been modified by involving overset meshes and the capability of this methodology to conduct flexibility studies involving complex flapping insect motion is currently being explored.

With the flexibility and accuracy of these open-source software and the ease with which complex simulations can be conducted, it has been established that this model is a viable choice for conducting research involving complicated mechanisms occurring in multi-physics problems such fluid-structure interaction like in insect flight aerodynamics.

References

- [1] S. P. Sane., “The aerodynamics of insect flight,” *The Journal of Experimental Biology*, vol. 4191, 2003.
- [2] K. Altaf, Aziz, Chen, Yunfei, Zhao, Nan, Alouini, Mohamed-Slim, Dobbins, and Paul, “A survey of channel modeling for uav communications,” *eprint arXiv:1801.07359*.
- [3] M. Sun and J. Tang, “Unsteady aerodynamic force generation by a model fruit fly wing in flapping motion,” *The Journal of Experimental Biology*, vol. 205, pp. 55–70, 2002.
- [4] D. Walle, B. Fidan, A. Sutton, Yu, Changbin, and D. Anderson, “Non-hierarchical uav formation control for surveillance tasks,” *10.1109/ACC.2008.4586587*, pp. 777–782, 2008.
- [5] C. P. Ellington, “The aerodynamics of insect flight,” *Philosophical Transactions of the Royal Society London*, vol. B 305, pp. 1–15, 17–40, 41–78, 1984.
- [6] A. P. Willmott and C. P. Ellington, “The mechanics of flight in the hawkmoth *manduca sexta*. ii. aerodynamic consequences of kinematic and morphological variation,” *The Journal of Experimental Biology*, vol. 200, pp. 2693–2704, 1997-2000.
- [7] A. R. Ennos, “The kinematics and aerodynamics of the free flight of some diptera,” *The Journal of Experimental Biology*, vol. 142, pp. 87–95, 1989.
- [8] G. Ruppell, “Kinematic analysis of symmetrical flight manoeuvres of odonata,” *The Journal of Experimental Biology*, vol. 144, pp. 13–43, 1989.
- [9] R. Srygley and A. Thomas, “Unconventional lift-generating mechanisms in free-flying butterflies,” *Nature*, vol. 420, pp. 600–664, 2002.
- [10] R. Dudley, “The biomechanics of insect flight,” *The Journal of Experimental Biology*, vol. 159, pp. 335–357, 2000.
- [11] M. F. M. Osborne, “Aerodynamics of flapping flight with application to insects,” *The Journal of Experimental Biology*, vol. 28, pp. 221–245, 1950.
- [12] M. Jensen, “Biology and physics of locust flight. iii the aerodynamics of locust flight,” *Philosophical Transactions of the Royal Society London Biology*, vol. 239, pp. 511–552, 1956.
- [13] G. Ribak, S. Barkan, and V. Soroker, “The aerodynamics of flight in an insect flight-mill,” *PLoS ONE 12(11)*, vol. e0186441.
- [14] M. H. Dickinson and K. G. Götz, “Unsteady aerodynamic performance of model wings at low reynolds numbers,” *The Journal of Experimental Biology*, vol. 174, pp. 45–64, 1993.

- [15] M. H. Dickinson, F. O. Lehmann, and S. P. Sane, “Wing rotation and the aerodynamic basis of insect flight,” *The Journal of Experimental Biology*, vol. 182, pp. 173–189, 1999.
- [16] H. Liu, C. P. Ellington, K. Kawachi, C. Van den Berg, and A. Willmott, “A computational fluid dynamic study of hawkmoth hovering,” *The Journal of Experimental Biology*, vol. 201, pp. 461–477, 1998.
- [17] C. Itai, C. Samuel, Whitehead, and B. Tsevi, “Fluid dynamics and control of insect flight,” *Nature Reviews Physics* 1, vol. 11, pp. 638–39, 2019.
- [18] M. Smith, P. Wilkin, and M. Williams, “The advantages of an unsteady panel method in modeling the aerodynamic forces on rigid flapping wings,” *The Journal of Experimental Biology*, vol. 199, pp. 1073–1083, 1996.
- [19] H. Liu and K. Kawachi, “A numerical study of insect flight,” *Journal of Computational Physics*, vol. 146, pp. 124–156, 1998.
- [20] T. Weis-Fogh, “Quick estimates of flight fitness in hovering animals, including novel mechanisms for lift production,” *The Journal of Experimental Biology*, vol. 59, pp. 169–230, 1973.
- [21] M. Lighthill, “On weis-fogh mechanism of lift generation,” *J. Fluid Mech*, vol. 60, pp. 1–17, 1973.
- [22] P. B. Walker, “Experiments on the growth of circulation about a wing and an apparatus for measuring fluid motion,” *Rep. Memo. Aeronaut. Res. (Great Britain)*, 1931.
- [23] T. Maxworthy, “Experiments on the weis-fogh mechanism of lift generation by insects in hovering flight. part 1. dynamics of the ‘fling’,” *The Journal of Fluid Mechanics*, vol. 93, pp. 47–63, 1979.
- [24] L. I. Sedov, *Two-Dimensional Problems in Hydrodynamics and Aerodynamics*. New York: Interscience Publishers, 1965.
- [25] S. Vogel, *Life in Moving Fluids*. Princeton, NJ: Princeton University Press, 1994.
- [26] M. Kramer, “Die zunahme des maximalauftriebes von tragflugeln bei plötzlicher anstellwinkelvergrosserung (boeneffekt),” *Combustion and Flame*, vol. 23, pp. 185–189, 1932.
- [27] L. Zhao, Q. Huang, and S. P. Deng, X. Sane, “Aerodynamics effects of flexibility in flapping wings,” *Journal of Royal Society Interface*, vol. 7, p. 485–497, 2010.
- [28] K. Deepa and K. Chang-kwon, “An analytical model and scaling of chordwise flexible flapping wings in forward flight.,” *iopscience*, 2017.
- [29] R. J. Wootton, “Leading edge section and asymmetric twisting in the wings of flying butterflies,” *Journal of Experimental Biology*, vol. 180, p. 105–117, 1993.
- [30] R. J. Wootton, R. C. Herbert, P. G. Young, and K. E. Evans, “Approaches to the structural

modelling of insect wings,” *Philosophical Transactions of the Royal Society London, Biology*, vol. 358, p. 1577–1587, 2003.

- [31] S. A. Combes and T. L. Daniel, “Flexural stiffness in insect wings,” *The Journal of Experimental Biology*, vol. 206, pp. 2979– 2987, 2989–2997, 2003.
- [32] L. Zhao, Q. Huang, X. Deng, and S. P. Sane, “Aerodynamic effects of flexibility in flapping wings,” *Journal of The Royal Society Interface*, vol. 7, no. 44, pp. 485–497, 2010.
- [33] D.-w. Peng and M. Milano, “Lift generation with optimal elastic pitching for a flapping plate,” *Journal of Fluid Mechanics*, vol. 717, p. R1, 2013.
- [34] Y. Liu, B. Cheng, Sanjay, S. Sane, and Deng, “Aerodynamics of dynamic wing flexion in translating wings,” *Experiments in Fluids*, vol. 56, 06 2015.
- [35] Y. Jin, J.-T. Kim, L. Hong, and L. P. Chamorro, “Flow-induced oscillations of low-aspect-ratio flexible plates with various tip geometries,” *Physics of Fluids*, vol. 30, no. 9, p. 097102, 2018.
- [36] S. Y. Shinde and J. H. Arakeri, “Physics of unsteady thrust and flow generation by a flexible surface flapping in the absence of a free stream,” *Proceedings of the Royal Society A: Mathematical, Physical and Engineering Sciences*, vol. 474, no. 2218, p. 20180519, 2018.
- [37] J. E. Bluman, M. K. Sridhar, and C.-k. Kang, “Chordwise wing flexibility may passively stabilize hovering insects,” *Journal of The Royal Society Interface*, vol. 15, no. 147, p. 20180409, 2018.
- [38] P. D. Yeh and A. Alexeev, “Free swimming of an elastic plate plunging at low reynolds number,” *Physics of Fluids*, vol. 26, no. 5, p. 053604, 2014.
- [39] N. Arora, C.-K. Kang, W. Shyy, and A. Gupta, “Analysis of passive flexion in propelling a plunging plate using a torsion spring model,” *Journal of Fluid Mechanics*, vol. 857, p. 562–604, 2018.
- [40] N. Lee, S. Lee, H. Cho, and S. Shin, “Effect of flexibility on flapping wing characteristics in hover and forward flight,” *Computers Fluids*, vol. 173, pp. 111 – 117, 2018.
- [41] “Openfoam user guide,” *CFD Direct*, vol. 7, 2019.
- [42] G. Dhondt, *The Finite Element Method for Three-Dimensional Thermomechanical Applications*. Wiley, 2004.
- [43] H. Bungartz, F. Lindner, B. Gatzhammer, M. Mehl, A. Scheufele, K. and Shukaev, and B. Uekermann, “precice—a fully parallel library for multi-physics surface coupling,” *Computers and Fluids*, vol. 141, pp. 250–258, 2003.
- [44] G. Hou, J. Wang, and A. Layton, “Numerical methods for fluid-structure interaction a

review,” *Communications in Computational Physics*, vol. 12, no. 2, pp. 337–377, 2012.

- [45] S. Deng, T. Xiao, M. Percin, B. van Oudheusden, H. Bijl, and B. Remes, *Numerical simulation of an X-wing flapping wing MAV by means of a deforming overset grid method*.
- [46] F. Togashi, Y. Ito, and M. Murayama, *Flow simulation of flapping wings of an insect using overset unstructured grid*.
- [47] K.-H. Kao, M.-S. Liou, and C.-Y. Chow, “Grid adaptation using chimera composite overlapping meshes,” *AIAA Journal*, vol. 32, no. 5, pp. 942–949, 1994.
- [48] M. Coutanceau and R. Bouard, “Experimental determination of the main features of the viscous flow in the wake of a circular cylinder in uniform translation. part 1. steady flow,” *Journal of Fluid Mechanics*, vol. 79(02), pp. 231–256, 1977.
- [49] T. DJ., “Experiments on the flow past a circular cylinder at low reynolds numbers,” *Journal of Fluid Mechanics*, vol. 19(01), pp. 60–80, 1964.
- [50] S. Dennis and G.-Z. Chang, “Numerical solutions for steady flow past a circular cylinder at reynolds numbers up to 100,”
- [51] F. Nieuwstadt and H. Keller, “Viscous flow past circular cylinders,” *Computers and Fluids*, vol. 1, pp. 59–71, 1973.
- [52] K. Hejranfar and E. Ezzatneshan, “Implementation of a high-order compact finite-difference lattice boltzmann method in generalized curvilinear coordinates,” *Journal of Computational Physics*, vol. 267, pp. 28–49, 2014.
- [53] C. Liu, X. Zheng, and C. Sung, “Preconditioned multigrid methods for unsteady incompressible flows,” *Journal for Computational Physics*, vol. 139(1), pp. 35–57, 1998.
- [54] D. Calhoun, “A cartesian grid method for solving the two-dimensional streamfunction-vorticity equations in irregular regions,” *Journal of Computational Physics*, vol. 176(2), pp. 231–275, 2002.
- [55] D. Russell and Z. Wang, “A cartesian grid method for modeling multiple moving objects in 2d incompressible viscous flow,” *Journal of Computational Physics*, vol. 191(1), pp. 177–205, 2003.
- [56] P.-H. Chiu, R.-K. Lin, and T. Sheu, “A differentially interpolated direct forcing boundary method for predicting incompressible navier-stokes equations in time-varying complex geometries,” *Journal of Computational Physics*, vol. 229(12), pp. 4476–4500, 2010.
- [57] H. Hamdani and M. Sun, “Aerodynamic forces and flow structures of an airfoil in some unsteady motions at small reynolds number,” *Acta Mechanica*, vol. 145, pp. 173–187, 2000.
- [58] K. Bishopp and D. Drucker, “Large deflection of cantilever beams,” *Quarterly of Applied Mathematics*, vol. 10, pp. 213–225, 1952.

Mathematics, vol. 3, no. 3, pp. 272–275, 1945.

- [59] V. Vázquez and J. Gerardo, “Nonlinear analysis of orthotropic membrane and shell structures including fluid-structure interaction.,” 2007.
- [60] S. Turek, J. Hron, M. Madlik, M. Razzaq, H. Wobker, and J. Acker, “Numerical simulation and benchmarking of a monolithic multigrid solver for fluid-structure interaction problems with application to hemodynamics. fluid structure interaction ii: Modelling, simulation, optimization,” *Springer Berlin Heidelberg*, p. 432, 2010.
- [61] L. A. Miller and C. S. Peskin, “When vortices stick: an aerodynamic transition in tiny insect flight.,” *The Journal of experimental biology*, vol. 207 Pt 17, pp. 3073–88, 2004.
- [62] Z. Jane Wang, “Two dimensional mechanism for insect hovering,” *Phys. Rev. Lett.*, vol. 85, pp. 2216–2219, Sep 2000.